UC Berkeley
UC Berkeley Electronic Theses and Dissertations

Title
Material and Optical Design Rules for High Performance Luminescent Solar Concentrators

Permalink
https://escholarship.org/uc/item/04p1p3zj

Author
Bronstein, Noah

Publication Date
2015

Peer reviewed|Thesis/dissertation

eScholarship.org Powered by the California Digital Library
University of California

Material and Optical Design Rules for High Performance Luminescent Solar Concentrators

By

Noah Dylan Bronstein

A dissertation submitted in partial satisfaction of the

requirements for the degree of

Doctor of Philosophy

in

Chemistry

in the

Graduate Division

of the

University of California, Berkeley

Committee in charge:

Professor A. Paul Alivisatos, Chair

Professor Peidong Yang

Professor Eli Yablonovitch

Fall 2015

Abstract

Material and Optical Design Rules for

High Performance Luminescent Solar Concentrators

by

Noah Dylan Bronstein

Doctor of Philosophy in Chemistry

University of California, Berkeley

Professor A. Paul Alivisatos, Chair

This dissertation will highlight a path to achieve high photovoltaic conversion efficiency in luminescent solar concentrators, devices which absorb sunlight with a luminescent dye and then re-emit it into a waveguide where it is ultimately collected by a photovoltaic cell. Luminescent concentrators have been studied for more than three decades as potential low-cost but not high efficiency photovoltaics. Astute application of the blackbody radiation law indicates that photonic design is necessary to achieve high efficiency: a reflective filter must be used to trap luminescence at all angles while allowing higher energy photons to pass through. In addition, recent advances in the synthesis of colloidal nanomaterials have created the possibility for lumophores with broad absorption spectra, narrow-bandwidth emission, high luminescence quantum yield, tunable Stokes shifts and tunable Stokes ratios. Together, these factors allow luminescent solar concentrators to achieve the optical characteristics necessary for high efficiency.

We have fabricated and tested the first generation of these devices. Our experiments demonstrate that the application of carefully matched photonic mirrors and luminescent quantum dots can allow luminescent concentration factors to reach record values while maintaining high photon collection efficiency. Finally, the photonic mirror dramatically mitigates the negative impact of scattering in the waveguide, allowing efficient photon collection over distances much longer than the scattering length of the waveguide.

After demonstrating the possibility for high performance, we theoretically explore the efficacy of luminescent concentrators with dielectric reflectors as the high-bandgap top-junctions in two-junction devices. Simple thermodynamic calculations indicate that this approach can be nearly as good as a traditional vertically stacked tandem. The major barriers to such a device are the optical design of narrow-bandwidth, angle-insensitive reflectors with near-unity reflectivity in the reflection band and near unity transmissivity in the pass-band. Additionally, lumophores with narrow emission line widths and carefully controlled Stokes shifts are required. If new lumophores and optical designs can be created that meet the demanding needs of this application, high performance two-junction photovoltaics that collect both the direct and diffuse light could be achieved.

Acknowledgements

Thanks to the family and friends who supported me during my doctoral studies. Your patience and support over the last five and a half years have made many late nights in the lab a little less lonely, and helped me keep a healthy balance.

Thanks to Lanfang Li, Yuan Yao, and Lu Xu for your tireless work making and testing luminescent concentrator devices. Without your efforts, this work would not have been possible. Also, thanks to Erin O'Brien, Alex Powers, Joe Swabeck, and Brent Koscher for contributing vast quantities of time to quantum dot synthesis and characterization.

Thanks to my advisor, Paul Alivisatos, for giving me the freedom to choose my own path, for better or worse, and for sharing the joy of science. And finally, thank you to Eli Yablonovitch for teaching me to accept what nature gives me – the truth has set me free.

Table of Contents

Chapter 1 : Introduction 1
1.1: Motivation 1
1.2: Operating Mechanism of Luminescent Solar Concentrators 1
1.3: Power Conversion in Luminescent Solar Concentrators 3
Chapter 2 : Material Design 7
2.1: Desired Absorption Spectrum 7
2.2: Semiconductor Heterostructure Nanoparticles 8
2.3: CdSe/CdS Seeded Nanorods 9
2.3.1: Synthesis 9
2.3.2: Characterization 11
2.3.3: Performance in Devices 18
2.4: CdSe/CdS Core/Shell Particles 22
2.4.1: Synthesis 24
2.4.2: Characterization 25
2.5: Measurement of Luminescence Quantum Yield 27
Chapter 3 : Optical Design 32
3.1: Desired Absorption Spectrum 32
3.2: Simulations 34
3.2.1: Monte-Carlo Simulation 34
3.2.2: Generalized Finite Element Photon Transport Model 37
3.3: Dielectric Multilayers 40
3.4: Performance in Devices 45
Chapter 4 : Luminescent Solar Concentrators as Top Junctions for Silicon 52
4.1: Thermodynamics 52
4.2: Performance predictions for real devices 54

List of Figures

Figure 1.1: The Working Mechanism of a Luminescent Solar Concentrator 2
Figure 2.1: Desired absorption spectrum of a luminescent solar concentrator 7
Figure 2.2 TEMs of CdSe/CdS nanorod size series 11
Figure 2.3: Sizing histograms for the CdSe/CdS nanorods in Table 12
Figure 2.4: Sizing histograms for CdSe/CdS nanorods in Table 13
Figure 2.5: Representative TEM micrograph scaled-up CdSe/CdS nanorods 13
Figure 2.6: Absorption and PL spectra of CdSe seeds and CdSe/CdS nanorods 14
Figure 2.7: Absorption and PL spectra of nanorod size series 15
Figure 2.8: Photoluminescence decay of CdSe/CdS nanorods 16
Figure 2.9: Time resolved luminescence spectrum of 93x9 nm CdSe/CdS nanorods 17
Figure 2.10: PLQY and PL decay times of CdSe/CdS nanorods 18
Figure 2.11: Schematic of fabricated LSC waveguides 19
Figure 2.12: Normalized EQE spectra of LSCs with nanorod loading series 20
Figure 2.13: Normalized EQE spectra of LSCs with nanorod size series 20
Figure 2.14: Propagation length of luminescence in the LSC 21
Figure 2.15: Schematic for path-length provided by scattering back-reflector 22
Figure 2.16: Extinction ratio calculations for a variety of core and shell sizes 23
Figure 2.17: Extinction spectrum of CdSe/CdS core/shell particles 24
Figure 2.18: Representative TEMs of CdSe/CdS core/shell particles 25
Figure 2.19: TEM micrographs showing faceting of 8 nm particles 25
Figure 2.20: Measured extinction ratios for CdSe/CdS core/shell quantum dots 26
Figure 2.21: PLQY for a range of CdS shell thicknesses on 3.5 nm CdSe cores 27
Figure 2.22: Schematic of the integrating sphere luminescence spectrometer 28
Figure 2.23: Calibration of the integrating sphere luminescence spectrometer 28
Figure 2.24: Spectral sensitivity of the integrating sphere luminescence spectrometer 31
Figure 2.25: Calibrated PLQY measurement of rhodamine 590 and 640 31
Figure 3.1: Desired absorption spectrum of the LSC 33
Figure 3.2: Scaling laws in transport-limited LSCs 33
Figure 3.3: Control flow of the Monte-Carlo LSC simulation 36
Figure 3.4: Paths and processes in the Monte-Carlo simulation 36
Figure 3.5: Comparison of Monte-Carlo simulation to experiment 37
Figure 3.6: Finite-element Beer-Lambert solver 39
Figure 3.7: Generalized LSC performance modeling 40
Figure 3.8: 1-d photonic crystal omnidirectional reflector 41
Figure 3.9: Bandwidth of omnidirectional 1-d reflector 42
Figure 3.10: Device stack using dielectric omnidirectional reflector 43
Figure 3.11: Reflectance of a Bragg mirror versus PL of nanorods 44
Figure 3.12: Layer thickness dependence of Bragg mirror reflectance 44
Figure 3.13: Simulated LSC devices with simulated mirrors 45
Figure 3.14: Measured reflectance of fabricated dielectric mirror 46

Figure 3.15: Angle-averaged reflectance of fabricated dielectric mirror 46
Figure 3.16: Device scheme for LSC with dielectric mirror 47
Figure 3.17: LSC device performance with dielectric mirror..... 48
Figure 3.18: Champion LSC device performance with dielectric mirror 48
Figure 3.19: Photon transport measurement in cloudy LSC with mirror 49
Figure 3.20: Photon transport measurements in clear LSC with mirror 49
Figure 4.1: LSC on Silicon tandem device architecture 52
Figure 4.2: Two-junction PV thermodynamic limit 53
Figure 4.3: Thermodynamic efficiency of the LSC-Silicon tandem..... 54
Figure 4.4: Photon flow model for LSC-Si tandem device 55

List of Tables

Table 1: Synthesis conditions for the series of CdSe/CdS nanorods..... 12
Table 2: Champion LSC device performance..... 47
Table 3: Power generation estimates for LSC+InGaP-Si tandem 56
Table 4: Power generation estimates for LSC+GaAs-Si tandem..... 57

Chapter 1 : Introduction

1.1: Motivation

Solar energy technologies have many uses: they can be used to generate electricity in remote areas; they can be used to power space craft; they can be used to heat water; but by far the most important use is to generate electricity for the electric grid, reducing fossil fuel consumption and the carbon dioxide emissions that are poised to change the Earth's climate. The implications of climate change will not be discussed in this dissertation, other than as follows: anthropogenic climate change is going to disrupt the way of life of most people on the planet, and the effects will be overwhelmingly negative. Therefore, climate change should be avoided or reduced if possible. Electricity generation from solar irradiance is one of the most promising strategies for reducing carbon dioxide emissions in the near future. This dissertation will explore one technology aimed at improving the power production and deployment of solar photovoltaics.

In the 1950's, photovoltaic cells were invented to convert light into electricity[1]. The fundamental idea was to use a semiconductor to absorb sunlight above its bandgap, which generated excited electrons. The device was structured to allow low energy electrons to pass through on one side and high energy electrons to pass through on the other side. Then an excited electron would rush out the high-energy-selective side, and be replaced by an unexcited electron on the low-energy side. This resulted in a net voltage and current that produced power. These devices were dubbed "photovoltaics" due to the light-induced voltage. The thermodynamics of photovoltaics were solved in 1961 by Shockley and Quessier[2]. Under solar illumination, the maximum possible power output of a solar cell could be calculated by knowing the band-gap of the semiconductor absorbed material. This analysis indicates that silicon is a good choice of material because of its appropriate bandgap, leading to a great deal of research developing better silicon photovoltaic cells.

In the 1970's, semiconductor grade silicon was primarily being made for the budding microelectronics industry, and was far too expensive for photovoltaic application. Solar energy researchers responded to the economic reality of the time by proposing that solar cells could be less efficient than silicon but also dramatically less expensive[3,4]. One proposed method was to use fluorescent polymer waveguides to concentrate light onto traditional silicon solar cells[5–7]. These devices were initially called fluorescent planar concentrators and later became known as luminescent solar concentrators (LSC). While the economics of silicon solar panels have changed dramatically in the intervening four decades, LSCs may still play an important role in photovoltaic electricity production.

The aim of this dissertation is to describe recent innovations in LSCs and show how those innovations can work together to make a high efficiency solar photovoltaic.

1.2: Operating Mechanism of Luminescent Solar Concentrators

The general principle behind LSCs is illustrated in Figure 1.1: incident photons from the sun are absorbed by lumophores in a waveguide, and the emitted photons are guided via total internal reflection (TIR) to an adjacent solar cell where they are converted to electricity. The

thermodynamic limit of the concentration ratio (C), the ratio of the photon fluxes at the absorption energy (E_1) and emission energy (E_2), is approximated by[8]

Equation 1.1

$$C \leq \frac{E_2^3}{E_1^3} \exp\left(\frac{E_1 - E_2}{k_B T}\right)$$

Equation 1.1 indicates that C should increase exponentially with the difference in photon energies (often called the Stokes Shift). According to equation (1), for a Stokes Shift greater than 300 meV, C could exceed the geometric optical limit of 46,200 for direct solar radiation.

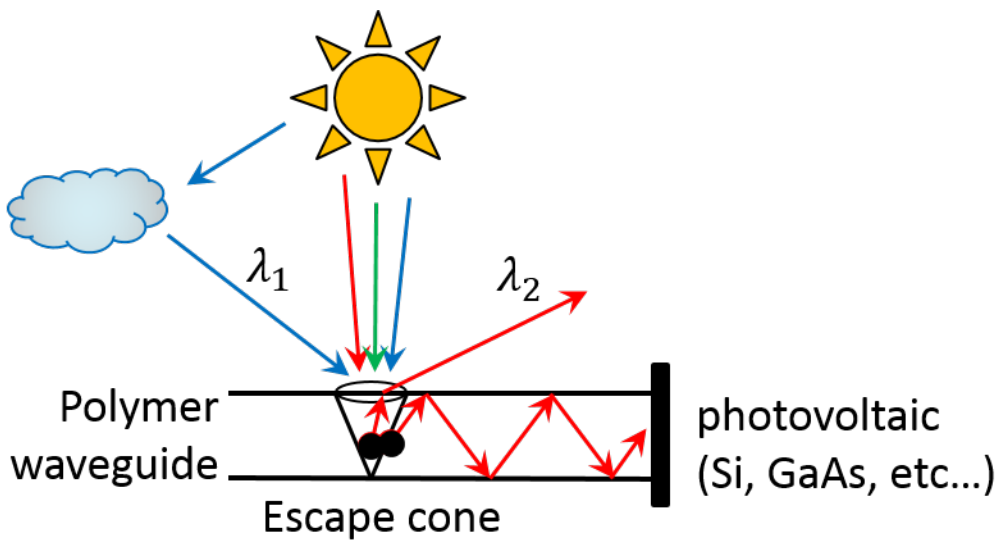

Figure 1.1: The Working Mechanism of a Luminescent Solar Concentrator
Broadband and diffuse solar illumination at high enters a polymer waveguide. The high energy photons ($\boldsymbol{\lambda_1}$) are absorbed by a lumophore, represented by the black circle. The lumophore re-emits the light at a lower energy, (longer wavelength, $\boldsymbol{\lambda_2}$). Due to the refractive index contrast between the waveguide and the surrounding medium, most of the luminesced photons are trapped by total internal reflection. The rest impinge on the front of the waveguide at angles inside the escape cone, allowing them to couple to the air. The trapped photons travel through the waveguide some long distance and then are captured by a photovoltaic cell, which produces electricity.

The concentration factor and collection efficiency achieved by LSCs to date has been limited due to parasitic losses such as non-unity quantum yields of the lumophores, imperfect light trapping within the waveguide, and reabsorption and scattering of propagating photons.[9] Previous studies have sought to solve each of these parasitic losses individually, resulting in modest performance improvements.[10–19] Research presented in this dissertation experimentally demonstrates a luminescent concentration ratio greater than 30 with an optical efficiency of 82% for blue photons by simultaneously addressing the materials and optical challenges of the LSC system[20,21]. These concentration ratios are achieved through the combination of designer quantum dot lumophores and photonic mirrors. To the best of our knowledge, this is the highest luminescent

concentration factor in literature to date. Previously, a concentration factor of 22 was reported in 1984 by Roncali and Garnier[16,22] using a dye with high luminescence quantum yield in a highly polished waveguide with mirrored edges. Such a strategy resulted in a low waveguide efficiency due to unmitigated escape cone losses. In contrast, our use of photonic mirrors that are carefully matched to narrow bandwidth emitting quantum dots lumophores allowed us to achieve waveguide efficiency exceeding the limit imposed by total internal reflection. Lessons learned from our design offer guidance towards the development of devices with both high concentration factors and high collection efficiencies.

Recent renewed interest in LSCs has been driven by materials research to overcome the reabsorption losses due to insufficient Stokes shifts, with particular emphasis on nanocrystal lumophores.[11] One such class of nanocrystals is the quantum dot heterostructure, where the effectives Stokes shift can be controlled by tuning either the core size or the thickness of the larger bandgap shell.[20,23,24] As the shell-to-core volume ratio increases, the overlap between absorption and emission decreases, thereby reducing reabsorption losses for luminesced photons traveling through the waveguide.[20]

1.3: Power Conversion in Luminescent Solar Concentrators

Like any solar photovoltaic, the goal of a luminescent solar concentrator is to produce electricity. Therefore, understanding the thermodynamic limits of converting sunlight into electricity in a LSC are crucial for guiding their development. Surprisingly little work has been done on the subject, but some basic principles can be understood without much difficulty.

Like any photovoltaic, the power produced by the LSC can be described by a current, voltage, and fill factor

Equation 1.2

$$P = V_{OC} J_{SC} FF$$

where V_{OC} is the open circuit voltage, J_{SC} is the short circuit current, and FF is the fill factor (which is generally between 0.8 and 0.9 for good photovoltaics). Below, I will describe how voltage and current are achieved in LSCs.

LSCs are in principle no different from other photovoltaic devices. That is, their ultimate efficiency in single-junction operation is well described by the very same analysis used by Shockley and Queisser. This method treats the internal workings of the LSC as a black box, and instead focuses on the amount of light absorbed and emitted by the LSC. The assumption made by Shockley and Queisser is that any absorbed photon can be converted to electric current. This assumption is a poor one for LSCs, which historically do not collect all the absorbed photons. The photocurrent available to the LSC can be described by the absorption spectrum multiplied by the incident solar flux

Equation 1.3

$$J_{SC} = \int_{\nu=0}^{\infty} \alpha(\nu, \mu, T) I(\nu) \eta_{coll} d\nu$$

where α is the absorption probability for incident photons at a given frequency ν in a semiconductor with temperature T and an excited carrier population with chemical potential μ (since the excited state population changes the absorption spectrum in some cases). I is the incident solar spectrum, and η_{coll} is the fraction of absorbed photons that are available as photocurrent. In general, the absorption spectrum and the solar spectrum are well understood, but η_{coll} is difficult to calculate. In principle it can be nearly unity, but in practice it is usually between 0.3 and 0.8, depending on the device configuration.

Once J_{SC} is determined, the voltage can be determined by following the Shockley-Queisser analysis as follows. At open circuit, no available photocurrent is extracted and so it is balanced by photoluminescence and nonradiative recombination. The luminescence spectrum (L) and intensity of the waveguide sheet are calculated from the absorption spectrum and an applied voltage[25,26] by multiplying the semiconductor blackbody spectrum (Equation 1.4) by the absorption spectrum according to Equation 1.5:

Equation 1.4

$$B(\nu,\mu,T) = \frac{2n^2\nu^2}{c^2} exp\left(\frac{\mu - h\nu}{k_B T}\right) d\Omega$$

Equation 1.5

$$L(\nu,\mu,T) = \alpha(\nu,\mu,T)B(\nu,\mu,T)$$

In Equation 1.4 and Equation 1.5, ν is the frequency of the photon, μ is the chemical potential of the photon field which is assumed to be equal to the voltage of the electrodes, T is the temperature of the electron and hole gas, n is the refractive index of the emissive medium (the waveguide polymer or the surrounding air), α is the absorption probability for incident photons at a given frequency, temperature, and chemical potential, c is the speed of light, and k_B the Boltmann constant. The current-voltage relationship is given by a modified version of the ideal diode equation:

Equation 1.6

$$J_0 = J_{rad} + J_{nr} = \frac{1}{ERE} \int_{\nu=0}^{\infty} \Omega_{PL} L(\nu,\mu,T) d\nu$$

Equation 1.7

$$J = J_{SC} - \frac{J_0}{ERE} e^{\frac{qV}{kT}}$$

In Equation 1.6, J_{rad} is the radiative current, J_{nr} is the non-radiative electrical current, Ω_{PL} is the solid angle of emission (typically π steradians), and ERE is the external radiative efficiency of the LSC waveguide. In Equation 1.7, V is the applied electrical bias. When the photon field and the electron-hole gas are in equilibrium, $\mu = qV$.

So far, this analysis of the voltage is unchanged from a standard flat plate solar cell. However, the picture becomes significantly more complicated due to the radiative coupling

between the LSC waveguide and the photovoltaic cell, which itself is subject to the same blackbody radiation laws described above.

The lessons available from this rudimentary analysis are useful in guiding the design of LSCs: (1) η_{coll} must be made as close to unity as possible to achieve maximum current, and (2) the voltage of the photovoltaic cell is determined by considering the luminescence energy and luminescence efficiency of the waveguide. While the first point is straightforward, the second warrants serious discussion in light of the radiative coupling between the LSC waveguide and the attached photovoltaic cell.

The luminescence collection efficiency η_{coll} is determined by three processes: absorbed photons must be luminesced, so the luminescence efficiency of the lumophore η_{PL} is important; the luminesced photons must travel through the waveguide to the photovoltaic cell, described by the efficiency $\eta_{waveguide}$; and they must be utilized by the active layer of that photovoltaic cell, described by the efficiency η_{abs}. Therefore, to a first approximation

Equation 1.8

$$\eta_{coll} = \eta_{PL}\eta_{waveguide}\eta_{abs}$$

The voltage is a more complicated matter. There are two ways to think about the voltage that are both helpful. First, in the limit of high efficiency, the above description regarding the external radiative efficiency of the waveguide and the luminescence energy of the lumophore is most appropriate. In this picture, both η_{PL} and η_{coll} approach unity. Additionally, the attached photovoltaic cell luminesces at an energy very near the luminescence energy of the lumophore with nearly unity efficiency. Then the life cycle of a photon entering the waveguide is prolonged: the photon enters the waveguide, is absorbed by the lumophore, is emitted by the lumophore, is absorbed by the photovoltaic cell, is emitted by the photovoltaic cell, is absorbed by either the lumophore or another photovoltaic cell, is emitted again, etc.… The process continues with reabsorption and reemission multiple times until eventually the photon escapes the waveguide as luminescence.

In practice, the photon recycling[27] described above is not seen in LSC waveguides. In fact, all LSC waveguides built to date use photons on average only once. In this low-performance limit, the voltage V is better described by considering the voltage of the photovoltaic cell under solar illumination, V_{AM15}, and applying the standard 60 mV per decade increase due to concentration factor C of light.

Equation 1.9

$$V = V_{AM15} + k_B T \ln\left(\frac{J_{LSC}}{J_{AM15}}\right) \approx V_{AM15} + k_B T \ln C$$

where J_{LSC} is the photocurrent achieved inside the LSC and J_{AM15} is the photocurrent under solar illumination. That is, the LSC waveguide acts to illuminate the photovoltaic device and photons on average do not come back to the LSC from the photovoltaic.

In general, the voltage achieved in the high-performance regime will be higher than the voltage achieved in the low performance regime, despite identical photocurrent production.

Unfortunately, the transition between the low-performance regime and the high-performance regime has never been the subject of a thorough thermodynamic treatment for luminescent solar concentrators, although it has been done for photovoltaic devices.[27,28] It is vitally important for future applications of LSCs to understand the relationship between various loss mechanisms and the power production of the LSC/PV system.

Chapter 2 will describe the use of customized quantum dot heterostructures to improve η_{coll} and C by reducing absorption at the luminescence energy.

Chapter 3 will describe our attempts to build devices that could be capable of photon recycling, improving η_{coll} and C through optical design.

Chapter 4 will describe calculations showing that if a sufficiently good LSC device can be built and put on top of another lower-bandgap photovoltaic, the resulting tandem device can have high photovoltaic efficiency.

Chapter 2 : Material Design

2.1: Desired Absorption Spectrum

The discussion in Chapter 1 about power generation and current collection shows that the ability to collect photons is at a premium: any high performing LSC must efficiently absorb sunlight, luminesce it at a lower energy, and guide the luminescence to a well matched photovoltaic cell. Optimizing this process has been the subject of virtually all research on LSCs in the past.

One cause for the poor performance of LSCs in literature is excessive overlap between lumophore absorption and emission spectra.[11] As a luminesced photon travels through the LSC, it may be reabsorbed by other lumophores. Every reabsorption event presents an opportunity for loss, such as non-radiative decay or emission into the escape cone. For this reason, LSC concentration ratios plateau long before the thermodynamic limit. This effect has been shown in recent work with inorganic lumophores,[29,30] organic lumophores in micro geometries with transfer-printed silicon[31,32] and GaAs solar cells,[33] as well as studied by numerical modeling.[12,34,35] To mitigate this loss mechanism, a lumophore with a narrow emission spectrum and a large Stokes shift is required. Literature studies of photon transport in LSCs were in the past hindered by a dearth of dyes meeting those criteria.[14,36] It is possible to calculate exactly the desired absorption spectrum, as follows.

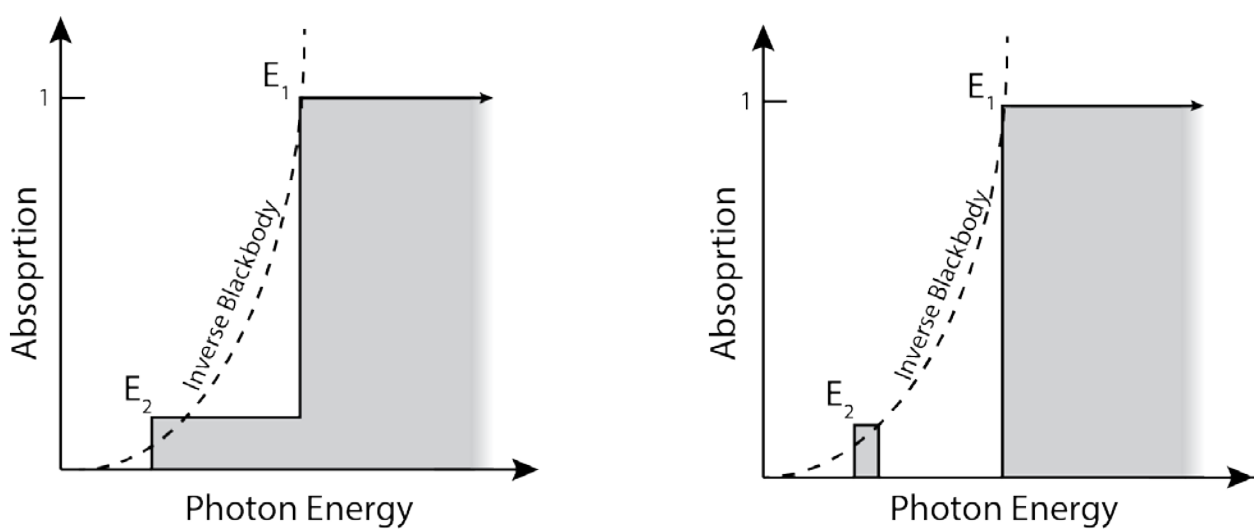

Figure 2.1: Desired absorption spectrum of a luminescent solar concentrator
The spectrum can either have two steps or a single bandgap with an optically active lower energy trap state. In both cases, the lower energy absorption must be large enough to overcome the Blackbody statistics that would cause undesirable high-energy luminescence.

The ideal material for a luminescent solar concentrator absorbs broadly above some threshold energy, and weakly at a lower energy. The desired absorption spectrum is either the sum

of two differently weighted Heaviside functions, or simply one Heaviside function with a small absorption feature at lower energy, as shown schematically in

Figure 2.1. The absorption should approach unity above the bandgap energy E_1 and then drop quickly enough to suppress emission from the band-tail. Mathematically, the absorption must have a slope steeper than the inverse of the blackbody factor described in Equation 1.4. At the lower energy E_2 the absorption must be somewhat larger than the inverse blackbody factor at that energy to allow the luminescence to be emitted at E_2 instead of E_1.

In practice, such absorption spectra are difficult to find in nature, and organic dyes will typically not exhibit this behavior. On the other hand, it is possible to engineer inorganic materials to have absorption spectra very near the desired absorption spectra. This chapter will discuss a strategy for synthesizing CdSe/CdS nanoparticle heterostructures with desirable absorption spectra. In addition, these particles are extensively characterized and their performance in built LSC devices is explored.

2.2: Semiconductor Heterostructure Nanoparticles

It is possible today to design a quantum dot system with a very high quantum yield, approaching unity, and the Stokes shift can be controlled by embedding the quantum dot emitter in a larger gap absorbing material. The entire dot system is still quite small compared to the emission wavelength, enabling low scattering. When compared to an organic dye molecule, the emission spectra of quantum dots are intrinsically narrower and more symmetric. This can be understood very qualitatively as arising from the extent of the delocalization of the electronic excitation. In the dye the excitation is confined to a much smaller volume, and hence leads to stronger coupling to vibrations, producing a larger Stokes shift. The volume of the excitation in a relevant quantum dot for a luminescent concentrator is on the order of 1000 times greater than in a corresponding dye.

The design scheme is simple, although its realization is often difficult: synthesize a high quality, low bandgap emitter material. Then grow a larger bandgap host matrix epitaxially around the emitter. So long as the host has type I band alignment,[37] both excited electrons and holes will tend to be trapped in the emitter material, and the luminescence efficiency will be high. By growing different quantities of host matrix, the relative absorption intensity of the two components can be tuned: thicker host matrix shells increase the absorption of the host, leaving the absorption of the core mostly unchanged. As the shell increases in thickness and absorption, fewer particles are needed to absorb incident light, which reduces the absorption of the low-bandgap material in the ensemble solid.

While in principle many semiconductor material pairs could have the desired absorption spectrum by utilizing this strategy, high luminescence yields are only routinely achieved with the CdSe core / CdS shell system. Many different shapes and sizes are routinely synthesized[38,39], and luminescence quantum yields approaching unity can be routinely achieved for some combinations of core size and shell thickness.[40] First we will explore CdSe/CdS dot/rod structures, and then CdSe/CdS core/shell “spherical” particles.

2.3: CdSe/CdS Seeded Nanorods

Size and shape control can be independently controlled in the CdSe/CdS system. Small (2-5 nm), high quality, highly monodisperse CdSe particles can be synthesized following literature methods.[39,41,42] The normal hot injection inverse micelle method uses a high-temperature solvent, cadmium bound strongly by nonpolar ligands, and a highly reactive Se precursor. The ligated cadmium mixture is brought to a high temperature in an air-free environment, and the Se precursor is injected rapidly. Precursor decomposition quickly saturates the solution, and a burst of nucleation then depletes the concentration of both Cd and Se.[43]

Once high quality CdSe particles are made, different sizes of CdS rods can be grown on those cores. The synthesis is very similar to the CdSe synthesis, but instead of generating a supersaturated solution that will nucleate new nanocrystals, the temperature is lowered to force growth onto existing CdSe seed crystals, which are injected along with the sulfur precursor. In our study, this was accomplished by injecting different quantities of CdSe cores into CdS growth solution following literature techniques.[44] Injecting fewer cores forces the CdS material to grow onto fewer particles, resulting in larger individual nanorods. The number of seeds used in each reaction is shown in Table 1, and the results are shown in Figure 2.2.

2.3.1: Synthesis

Chemicals and Synthetic Apparatus: CdO (Alfa Aesar, 99.998%), octadecylphosphonic acid (PCI, 99%), hexylphosphonic acid (PCI, 99%), trioctylphosphine oxide (Strem, 99%), selenium powder (Sigma Aldrich, 99.99%), sulfur chunks (Alfa Aesar, 99.9995%), trioctylphosphine (Strem, 97%), octylamine (Sigma Aldrich, 99%) were used as-purchased. Hexanes and acetone, used in particle cleaning, were obtained from a solvent still and stored over molecular sieves inside an argon-filled glovebox. All reactions were done using standard Schlenck line procedures. The Schlenck line used in these procedures has an argon line flowing through a Drierite® drying chamber and a vacuum line with a roughing pump with stable vacuum pressure of <100 mTorr. All post-synthetic cleaning procedures were performed by mixing solvents in an argon-filled glovebox and centrifugation with argon-filled centrifuge tubes, though the centrifuge is outside the glovebox.

Synthesis of CdSe Seeds: CdSe seeds were prepared by mixing 60 mg of CdO with 280 mg of octadecylphosphonic acid and 3.0 g of trioctylphosphine oxide in a 50 mL 3-neck flask with a ½" octagonal magnetic stir-bar, a glass thermocouple adapter sealed with H-grease, and a silicone septum port. The mixture was heated to 150°C under vacuum for 1 to 1.5 hours to degas, after which the flask is filled with argon and heated to 320°C for 1 to 2 hours, shaking occasionally to rinse all the CdO into the solution, until the solution is clear, and sometimes slightly yellow. After this complexation step, the solution is degassed at 150°C under vacuum for 1-2 hours, until the vacuum pressure recovers to 100 mTorr or lower. In an argon filled glovebox, 360 mg trioctylphosphine is stirred with 60 mg selenium powder for 1-2 hours, until the selenium has all dissolved. The three-neck flask is then heated to 380°C under argon, and with vigorous stirring (stir plate set at the highest setting) the TOP:Se mixture is injected from a 2 mL plastic syringe with a 2” 22 gauge needle. Immediately after injection, the reaction mixture is allowed to cool by removing the heating mantle and blowing air over the flask. Once the reaction solution reaches

110°C, 5 mL of hexanes and 2.5 mL of octylamine are injected and the reaction mixture is brought into the glovebox. The particles are precipitated with acetone and centrifuged at 8000 rpm for 10 minutes. The supernatant is discarded and the particles are redispersed in hexanes, leaving a cloudy white particulate floating in the vial. The solution is centrifuged at 8000 rpm for 10 minutes to remove the white particulate, and the supernatant is decanted. The supernatant is then precipitated again with acetone, centrifuged at 8000 rpm for 5 minutes. The precipitate is then dissolved in hexanes and stored in the glovebox. The particle size and concentration are determined from the wavelength and absorbance at the first exciton following the method of Yu et al.[45]

Large-Scale Seeded Growth of CdSe/CdS rods for loading-dependence*:* 400 mg CdO, 300 mg hexylphosphonic acid, 1450 mg octadecylphosphonic acid, and 15.0 g trioctylphosphine oxide are mixed in a 100 mL three-neck roundbottom flask with 1“ octagonal stir bar, glass thermocouple adapter sealed with H-grease, and silicone septum port. The mixture was heated to 230°C under vacuum for 15 minutes to degas, after which the flask is switched to argon and heated to 320°C for 1 to 2 hours, shaking occasionally to rinse all the CdO into the flask, until the solution is clear. After this complexation step, the solution is degassed at 150°C under vacuum for 2-4 hours, until the vacuum pressure recovers to 100 mTorr or lower. In an argon filled glovebox, 7.5 g trioctylphosphine is stirred with 600 mg sulfur for 2 hours, until the sulfur has all dissolved. CdSe particles are dried under vacuum to remove hexanes and dispersed in TOP (0.4 micromoles in 1.5 g). The three-neck flask is then heated to 340°C under argon, and with vigorous stirring (stir plate at the highest setting) the TOP:S mixture is injected from a 10 mL plastic syringe with a 5“ 18 gauge needle. After 20 seconds, the TOP+CdSe solution is injected rapidly. The temperature of the solution is maintained at 320°C for 5 minutes before the heating mantle is removed and the solution is allowed to cool slowly to 100 C, at which point 15 mL of hexanes is injected and the solution is brought into the glovebox for cleaning. The solution is precipitated with acetone and centrifuged at 8000 rpm for 10 minutes. The supernatant is thrown away and the particles are redispersed in hexanes, leaving a cloudy white particulate floating in the vial. The solution is centrifuged at 8000 rpm for 10 minutes to remove the white particulate, and the supernatant is decanted and stored in the glovebox over the weekend, as more white precipiate forms. The solution is centrifuged again at 8000 rpm for 10 minutes to remove the white precipitate. The supernatant is decanted and stored in the glovebox.

Seeded Growth of different sizes of CdSe/CdS rods*:* 500 mg CdO, 400 mg hexylphosphonic acid, 1450 mg octadecylphosphonic acid, and 15.0 g trioctylphosphine oxide are mixed in a 100 mL three-neck roundbottom flask with 1“ octagonal stir bar, glass thermocouple adapter sealed with H-grease, and silicone septum port. The mixture was heated to 150°C under vacuum for 10 minutes to degas, followed by 3 pump/purge cycles with argon, allowing the pressure to recover to less than 200 mTorr each time. The flask is then switched to argon and heated to 320°C for 1 hour, shaking occasionally to rinse all the CdO into the flask, until the solution is clear. After this complexation step, the solution is degassed at 150°C under vacuum for 2 hours, until the vacuum pressure recovers to 100 mTorr or lower. In an argon filled glovebox, 6 identical solutions of TOP:S are prepared by heating 1.5 g trioctylphosphine with 120 mg sulfur for 1 hour at 60°C with stirring, until the sulfur has all dissolved. CdSe particles are dried under vacuum to remove hexanes and dispersed in the TOP:S solutions. Different quantities of nanoparticles are added to each solution to allow the growth of different sizes of nanorods, as shown in Table . The cadmium solution is held at 100°C under argon for several hours as all the reactions are done in series, starting with sample A and going in order to F.

A 50 mL the three-neck flask with a ½" octagonal stir bar is held under vacuum and 3 mL of $Cd(ODPA)_2$+TOPO solution is added with a 3 mL syringe and a 5" 18 gauge needle. The flask is degassed by a few pump-purge cycles and then heated to 360°C under argon. With vigorous stirring (stir plate at the highest setting) the TOP:S+CdSe mixture is injected from a 10 mL plastic syringe with a 2" 22 gauge needle. The temperature of the solution drops to 330°C, but recovers to 360°C. 8 minutes after the injection, the heating mantle is removed and the solution is allowed to cool to 100 C, at which point 6 mL of hexanes is injected and the solution is brought into the glovebox for cleaning. The solution is precipitated with acetone and centrifuged at 8000 rpm for 10 minutes. The supernatant is thrown away and the particles are redispersed in hexanes and precipitated again with acetone. The solution is centrifuged at 8000 rpm for 10 minutes. The particles are then redispersed in 3 mL of hexanes with 2 drops of octylamine.

2.3.2: Characterization

The characterization required to be useful for a LSC is primarily optical: absorption and emission spectra are taken, and photoluminescence quantum yield (PLQY) is measured. In order to understand the structural reason behind any optical behavior, size and shape are analyzed with transmission electron microscopy (TEM). Representative TEM micrographs are shown in Figure 2.2. For each sample, hundreds of particles were analyzed by hand in ImageJ, and the size statistics are compiled in Table .

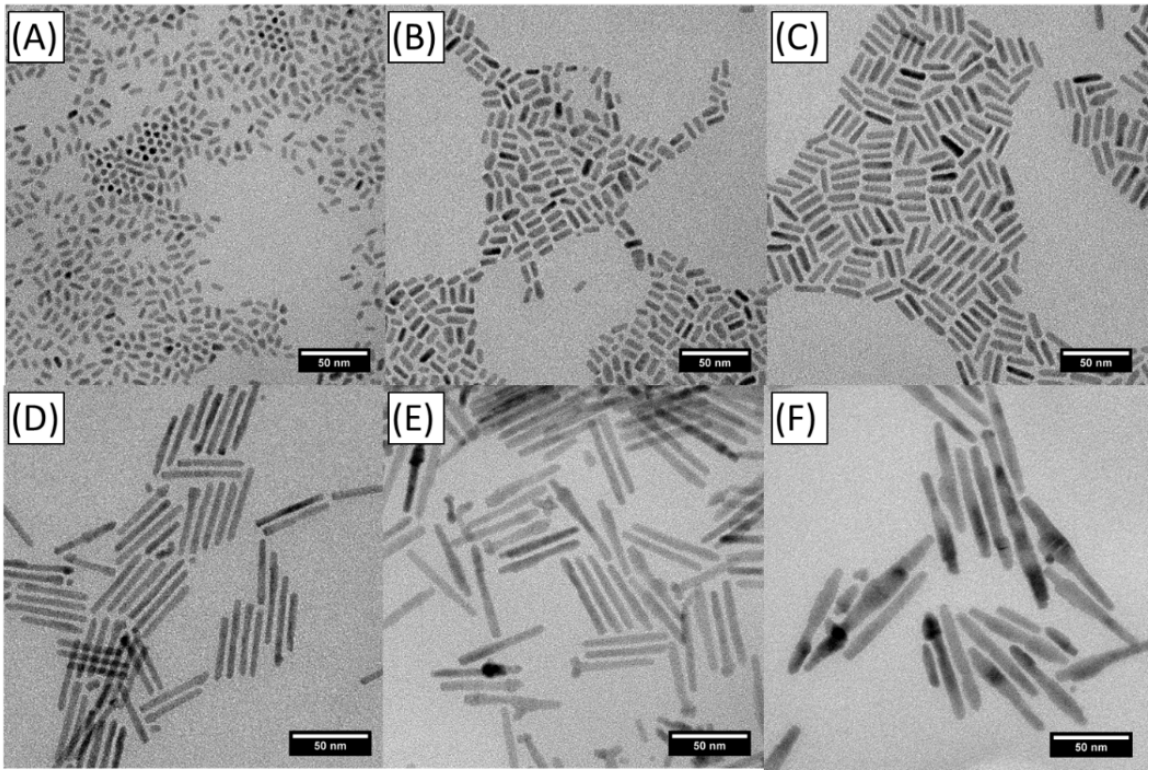

Figure 2.2 TEMs of CdSe/CdS nanorod size series
From left to right, fewer CdSe seeds were used in the synthesis, resulting in larger rod growth on each seed crystal. The sample letter codes overlaid on each micrograph will be used to described these samples throughout this text.

Sample	Moles of CdSe particles	Nanorod Length (nm)	Nanorod Width (nm)	Nanorod Volume (nm^3)
A	8E-8	8.8 ± 1.2	4.1 ± 0.6	119
B	4E-8	12.4 ± 2.0	4.9 ± 0.8	237
C	2E-8	21.5 ± 1.7	5.0 ± 0.7	426
D	1E-8	43.9 ± 7.4	4.7 ± 0.6	788
E	5E-9	55.6 ± 8.8	6.1 ± 1.1	1640
F	2E-9	78.2 ± 12.4	9.3 ± 2.3	5275

Table 1: Synthesis conditions for the series of CdSe/CdS nanorods

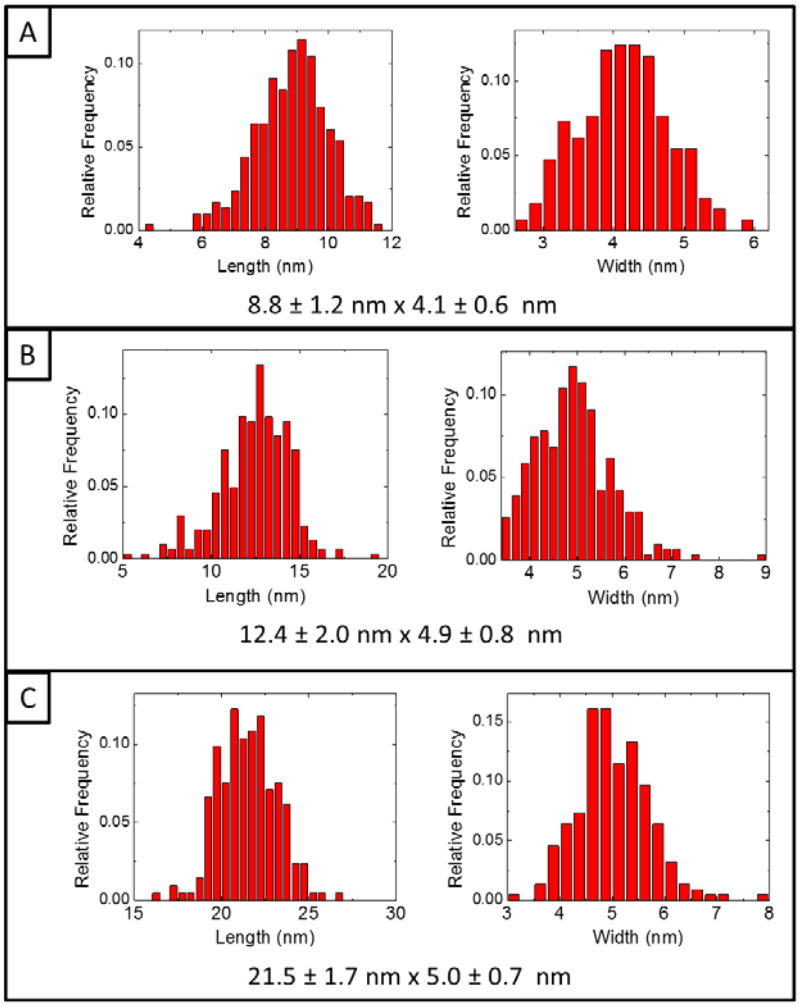

Figure 2.3: Sizing histograms for the CdSe/CdS nanorods in Table

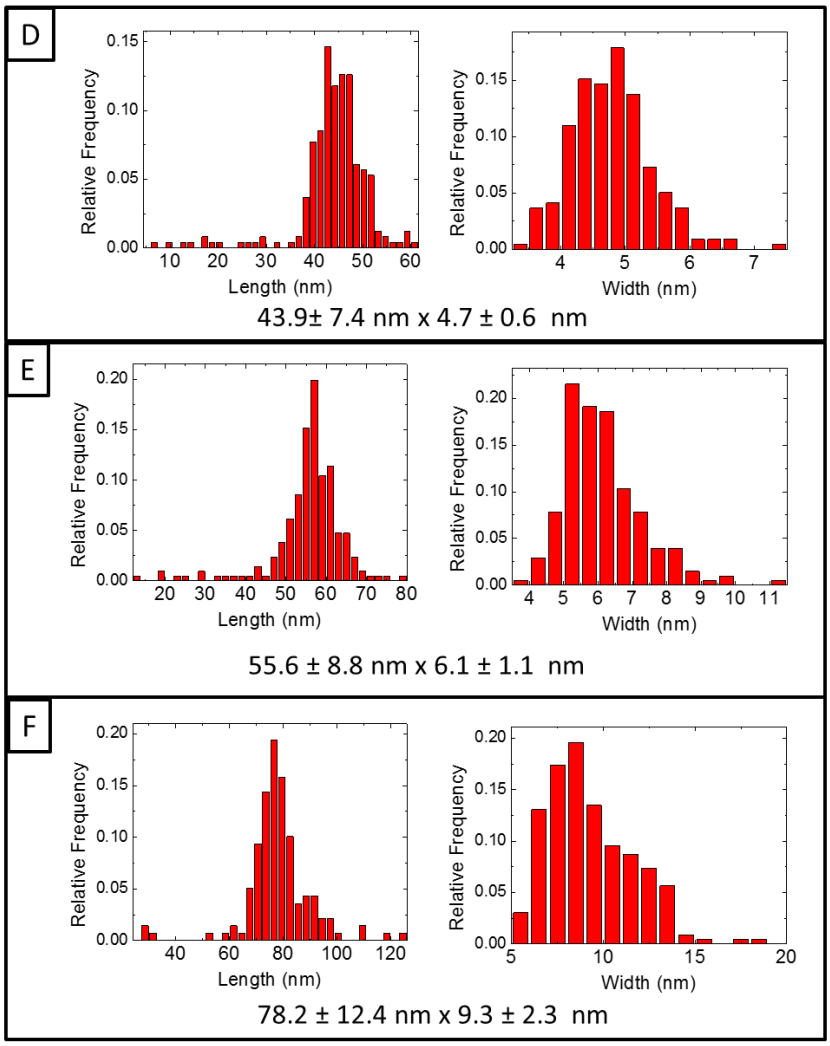

Figure 2.4: Sizing histograms for CdSe/CdS nanorods in Table

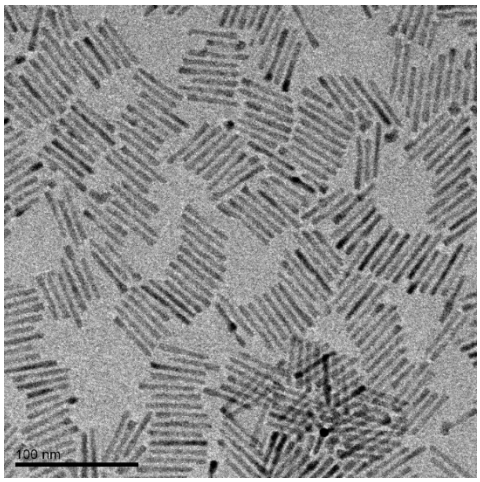

Figure 2.5: Representative TEM micrograph scaled-up CdSe/CdS nanorods
Nanorods were synthesized in a large-scale batch. Scale bar is 100 nm.

The absorption and photoluminescence (PL) spectra are measured by dissolving the particles in a nonpolar solvent like hexanes or toluene and diluting them into a 1 cm path length cuvette. Absorption spectra are taken using a Shimadzu UV3600 dual-beam absorption spectrometer, and luminescence spectra are taken with a Horiba Jobin-Yvon FluoroLog 2 with a monochromated Xenon excitation lamp. The absorption and PL spectra of the CdSe seeds and a typical CdSe/CdS dot/rod structure are shown in Figure 2.6 and the absorption and PL spectra of the set of CdSe/CdSe nanorods is found in Figure 2.7. The absorption spectra show that as the CdS rod is grown longer and fatter, a few effects can be seen: the CdS band edge shifts toward lower energy, approaching its bulk value, due to the loss of quantum confinement; the CdSe emission shifts toward lower energy as the electron is delocalized; and the ratio of the absorption at high energy (400 nm) to the absorption at the emission wavelength is dramatically increased, so that in the largest nanorods the low-energy absorption feature cannot be easily seen on the same linear scale as the CdS absorption.

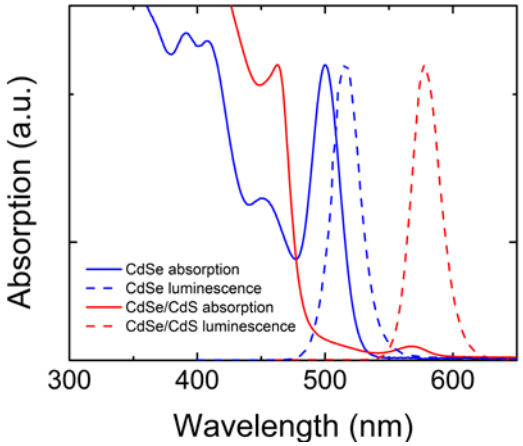

Figure 2.6: Absorption and PL spectra of CdSe seeds and CdSe/CdS nanorods
The CdSe cores show a typical quantum confined semiconductor absorption spectrum, with very little Stokes shift. The seeded nanorods show a two-step absorption spectrum, with the emission coming from the low energy CdSe part of the spectrum, and a large increase in absorption at the CdS band edge.

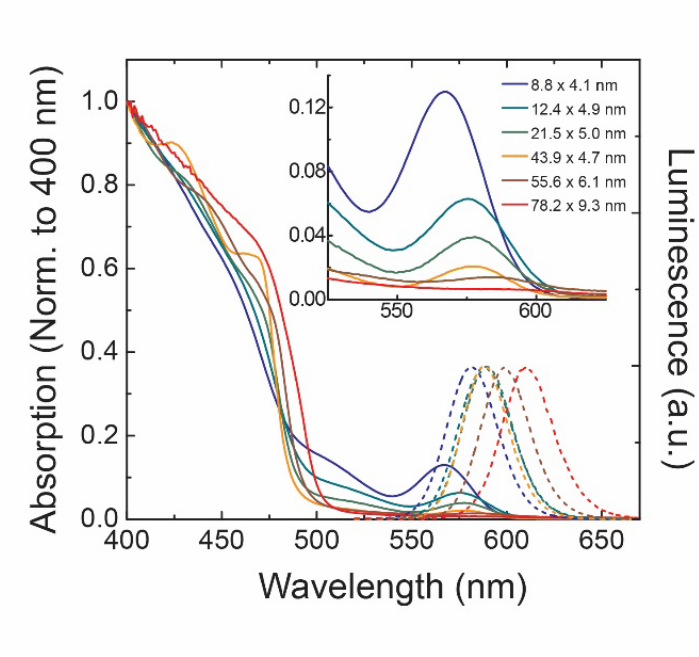

Figure 2.7: Absorption and PL spectra of nanorod size series
The larger nanorods show a slightly longer wavelength CdS absorption edge, due to the loss of quantum confinement as their diameter increases. They also show a longer wavelength emission from the CdSe core, and a decreased absorption at the CdSe core relative to the CdS rod material.

The luminescence lifetime was measured on a PicoQuant FluoTime300 using time-correlated single-photon counting. The detector is a chilled photomultiplier tube with <1 dark count per second, and the excitation source is a 407 nm pulsed diode laser with a <100 ps pulse width. The instrument response time, including all optics and electronics, is <150 ps. The results of this measurement can be found in Figure 2.8. The raw data were fit to triexponential decays, and the intensity weighted average was computed according to Equation 2.1 and Equation 2.2.

Equation 2.1

$$counts(t) = A_1 exp\left(-\frac{t}{\tau_1}\right) + A_2 exp\left(-\frac{t}{\tau_2}\right) + A_3 exp\left(-\frac{t}{\tau_3}\right)$$

Equation 2.2

$$\tau_{meas} = \frac{A_1\tau_1^2 + A_2\tau_2^2 + A_3\tau_3^2}{A_1\tau_1 + A_2\tau_2 + A_3\tau_3}$$

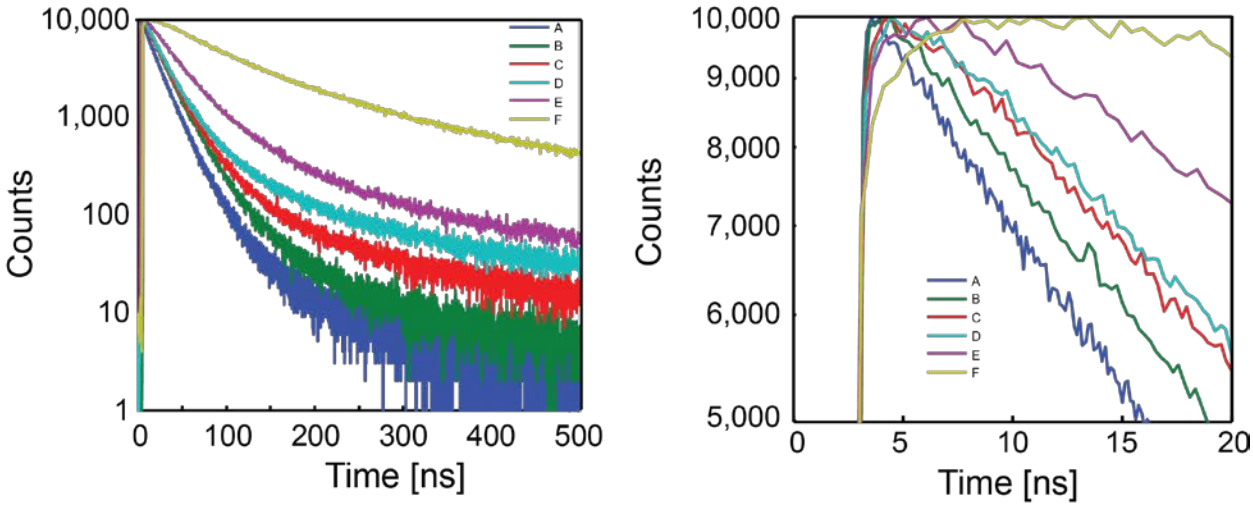

Figure 2.8: Photoluminescence decay of CdSe/CdS nanorods
The luminescence was measured at the peak luminescence wavelength with a 10 nm bandpass on the detection monochromator. The largest structures show a rise time of up to 5 ns for a fraction of the luminescence.

Examining the long time behavior in Figure 2.8, it is eminently clear that none of the particles demonstrate monoexponential decay kinetics. For some, the behavior might be modeled as biexponential with part of the decay happening at the radiative rate, and part happening at a much longer rate. However, for others two exponentials will not be enough, and a distribution of exponentials is more likely to be physically valid. In all cases, the curves can be fit with a triexponential decay, although there is no good physical interpretation for such a decay. Regardless, it is useful in order to provide a single average decay time for luminesced photons. The long-time behavior is likely due to the slow detrapping of charger carriers that, for whatever reason, end up trapped in mid-gap states far away from the band edge.

Examining the short time behavior in Figure 2.8 reveals even more complexity. While the smaller particles exhibit very rapid onset of the luminescence after the laser pulse, consistent with rapid thermalization of charge carriers, the longer rods do not. The largest rods exhibit a 5-10 ns rise time which only applies to about a third of the luminesced photons. This rise time implies that the photoexcited carriers do not rapidly thermalize all the way to the CdSe core in about a third of the absorption events. No ready explanation is at hand for this phenomenon. To attempt to gain better understanding of it, the PL spectrum over time was measured, as shown in Figure 2.9. At very short times after excitation, the luminescence is extremely broad band. The high energy luminescence decays much more rapidly than the low energy CdSe luminescence, with a time constant of around 1-5 nanoseconds. This decay time is slightly faster than the rise time of the CdSe luminescence. The two phenomena could arise from the same physical process. Further work would be required to prove a mechanism.

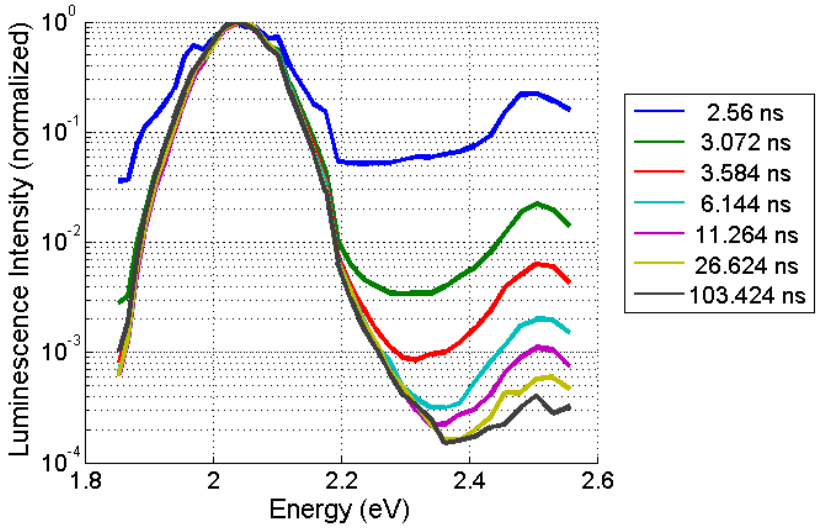

Figure 2.9: Time resolved luminescence spectrum of 93x9 nm CdSe/CdS nanorods
The spectra have been normalized to their peak value. The high dynamic range is afforded by varying the integration time and using neutral density filters.

Next, the photoluminescence quantum yield (PLQY), a crucial parameter for LSC application, was measured. The PLQY was measured with a Horiba Jobin-Yvon FluoroLog 3 and an integrating sphere attachment, calibrated with a NIST-traceable OceanOptics radiometric blackbody source. The detector in this instrument was a photomultiplier tube, and the measurements were taken three times each to ensure stability and reproducibility. The results of this measurement can be found in Figure 2.10. The luminescence quantum yield, in combination with the measured luminescence decay time (τ_{meas}), yields characteristic radiative (τ_{rad}) and nonradiative (τ_{nr}) lifetimes via

Equation 2.3

$$\tau_{rad} = \frac{\tau_{meas}}{PLQY}$$

Equation 2.4

$$\tau_{nr} = \frac{\tau_{meas}}{1 - PLQY}$$

The result shows that larger nanorods have worse luminescence quantum yields. The reason, in this case, is illuminated by the radiative rates, which increase linearly with the volume of the total structure. The radiative lifetime increases from around 35 ns for the smallest nanorods to nearly 1 us for the largest nanorods. The nonradiative rate slows at the same time due to the thickening of the CdS shell around the core, but not enough to counteract the dramatic increase in radiative lifetime due to the increasing shell volume.

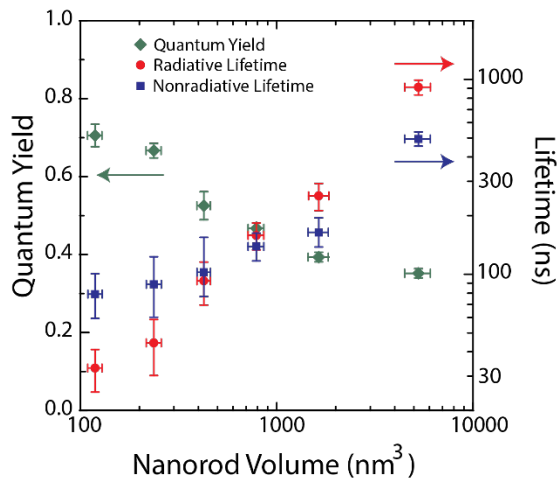

Figure 2.10: PLQY and PL decay times of CdSe/CdS nanorods
The radiative lifetime gets longer for larger nanorods, nearly linearly with the nanorod volume. The nonradiative rate also gets longer, but not as quickly. The overall result is a decrease in the luminescence quantum yield for larger CdS rods grown on the same CdSe core.

2.3.3: Performance in Devices

Due to the low luminescence quantum yield of these CdSe/CdS nanorods, they cannot make high performance LSC devices. However, the photon transport inside the LSC waveguide can still be investigated using the series of nanorods. The hypothesis is that the larger rods, due to the reduced absorption at the photoluminescence wavelength, should allow photons to travel longer distances in the LSC waveguide.

To study this phenomenon, LSC waveguides were fabricated with a small silicon photovoltaic device in the middle as a detector. The geometry of the waveguide is shown in Figure 2.11. There is a 30 um thick polymer with embedded nanorods on top of a 180 um glass plate. This entire device is suspended by an air gap over a 1 mm thick glass substrate. The waveguide thickness arises from the 210 micron combined thickness of the quartz plate and the polymer nanorod composite. The waveguide length is defined by the edge length of the square polymer film, which is 38 mm. The silicon PV detector built into the waveguide is 1.5 mm x 0.1 mm, making it small enough to act as a non-perturbative probe of the photon field.

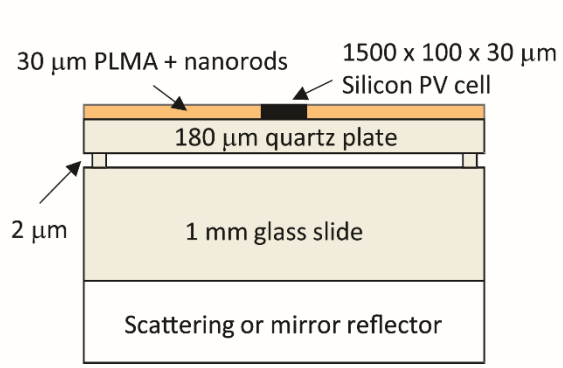

Figure 2.11: Schematic of fabricated LSC waveguides

The LSC waveguides were placed in a solar simulator, and the current-voltage characteristic of the silicon detector was measured. Several different nanorod polymer composites all resulted in somewhat different photocurrent, and the photocurrent was always higher than the waveguide without any nanorod.

To see where in the spectrum the photocurrent comes from, the external quantum efficiency (EQE) of the waveguide is measured by the embedded silicon detector with a large illumination spot (diameter around 15 mm). The convolution of inhomogeneous illumination with highly position-dependent collection efficiency (photons absorbed closer to the PV cell are more likely to strike the PV cell after luminescence) results in an EQE spectrum that is qualitative (it should be monotonically related to the true EQE). The results are normalized to the performance of the micro solar cell measured at 600 nm in the same geometry without any lumophore and without a reflective back surface. The device with no nanorods (OD=0) but with a reflective back surface is shown for comparison. The concentration can exceed 1 without nanorods but with a reflective back surface due to the angular spread of the light source in the measurement. Photons that enter the LSC at oblique angles near the solar cell can be reflected on to the solar cell. To maximize the probability that a photon travelling through the waveguide is absorbed in the photovoltaic cell, the polymer must not be much thicker than the photovoltaic cell itself, which is 30 um. To achieve optical density of 1 in the film, approximately 0.3% of the polymer volume must be displaced by nanorods.[46] Increasing the nanorod loading initially increases the concentration of light from the blue region of the spectrum, where the nanorods absorb, without concentrating light from the red region of the spectrum, where the nanorods do not absorb. Minimal scattering was observed at optical density up to 0.1 at 450 nm. However, above optical density 0.1, concentration of blue light decreases and concentration of red light increases because of the scattering of light in the waveguide, likely as a result of nanoparticle agglomeration.

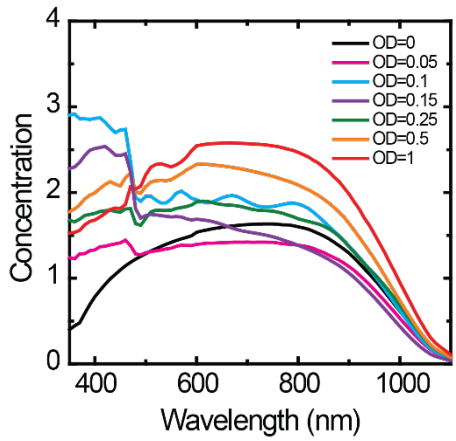

Figure 2.12: Normalized EQE spectra of LSCs with nanorod loading series
The absorption of the nanorods dominates from 350 to 500 nm. At longer wavelengths, scattering from nanorod aggregates leads to increased concentration of photons. Oscillations due to the 2 um air cavity can be seen in some cases when scattering is low.

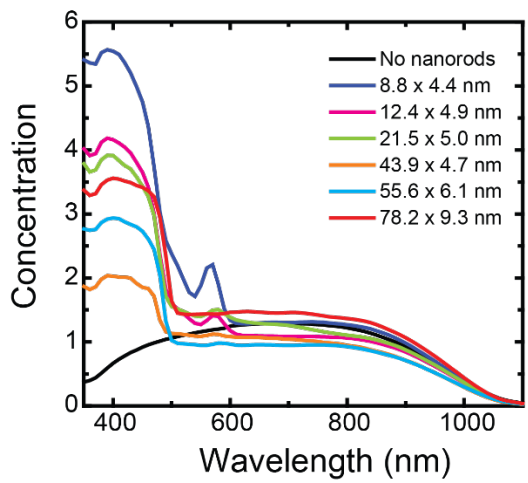

Figure 2.13: Normalized EQE spectra of LSCs with nanorod size series
The absorption of the nanorods dominates from 350 to 500 nm. At longer wavelengths, scattering from nanorod aggregates leads to increased concentration of photons.

Next, the series of nanorods of different sizes were incorporated into LSC waveguides. Optical density for these devices was held to around 0.1 at 450 nm to avoid the scattering apparent at higher loadings. This is accomplished by holding the volume fraction of CdS nearly constant. Large nanorods, then, are incorporated in fewer numbers than small nanorods. Figure 2.13 shows the concentration as a function of wavelength for the different nanorod sizes. In all cases, the concentration of blue photons in the device follows the absorption spectrum of the nanorods; the concentration of red photons is suppressed in each case, confirming minimal scattering of light in the LSC sheet.

The propagation of photons inside the waveguide was characterized by illumination in a solar simulator with an aperture controlling the illumination area. A blue band-pass filter centered

at 405 nm is used to isolate the luminescence of the nanorods from scattered red light. A circular aperture is centered on the silicon photovoltaic cell, and the photocurrent measured as a function of aperture radius. Figure 3(c) shows the results for the largest and smallest nanorods. The smallest nanorods show concentration that increases rapidly at small radii, but begins to asymptote at larger radii. In contrast, the larger nanorods show current that increases nearly linearly with increasing radius. The propagation of photons inside the waveguide can be approximated as an exponential decay with a characteristic length-scale known as the propagation length. Allowing for a short-propagating population of scattered photons and a long-propagating population of luminesced photons, the photocurrent is fit to the equation:

Equation 2.5

$$J_{photo}(r) = J_{max} - A_1 \exp\left(-\frac{r}{L_1}\right) - A_2 \exp\left(-\frac{r}{L_2}\right)$$

where $J_{photo}(r)$ is the measured photocurrent at an aperture radius r and the following parameters are a result of the curve fit: J_{max} is the photocurrent at infinite device size, L_1 and L_2 are propagation lengths for scattered and luminesced photons, respectively, with their associated magnitudes A_1 and A_2. This model is reasonable because the population of scattered photons must be generated on one pass through the LSC, requiring a characteristic scattering length on the order of the thickness of the LSC. As a result, scattered photons only travel a few hundred microns. In contrast, the luminesced photons have been shifted from their incident wavelength to the luminescent wavelength, allowing the different length scales for generation and propagation. The propagation length of the luminesced photons, plotted in Figure 2.14, shows increasing propagation length with increasing nanorod volume due to the reduced reabsorption from the CdSe seed.

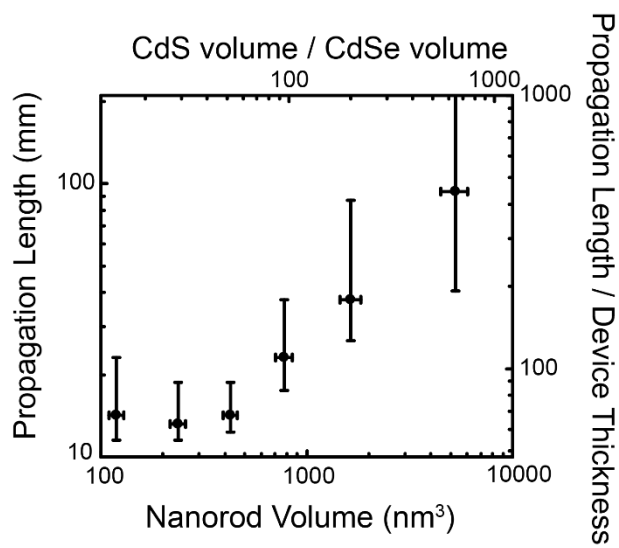

Figure 2.14: Propagation length of luminescence in the LSC
Error bars in the vertical direction represent fit error by a X^2 analysis, and error bars in the horizontal direction represent the distribution of particle sizes.

As a result of the limited optical density of the films, a reflective back surface is required to increase the absorption path-length. In this study, a black anodized aluminum surface, a silver mirror, and a scattering white Spectralon surface were used. The propagation lengths in Figure 2.14 are not significantly different for the different back surfaces. A black back surface allows 1 pass for absorption, a mirror back surface allows 2 passes, and a scattering surface allows 2.2 passes for a polymer with refractive index of 1.4, as the oblique rays bend back toward normal upon refraction into the polymer. The average value of 2.2 is calculated by averaging the path lengths of a hemispherical emission refracted through a higher index material, shown schematically in Figure 2.15.

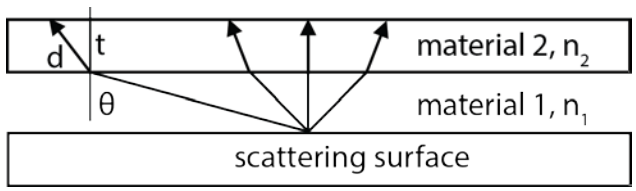

Figure 2.15: Schematic for path-length provided by scattering back-reflector

Equation 2.6

$$\frac{d_{avg}}{t} = 1 + \int_0^{\frac{\pi}{2}} \frac{2\cos(\theta)\sin(\theta)\,d\theta}{\cos\left(\arcsin\left(\frac{n_1}{n_2}\sin(\theta)\right)\right)}$$

While this optical path-length enhancement is less than the $4n^2$ Yablonovitch scattering limit of 7.8, that limit is only achieved by continual randomization of photons within the polymer, which would eliminate the long-travelling waveguide modes.[13,47] While it is still possible in theory to achieve luminescent concentration beyond the scattering limit in such a circumstance with the application of perfect light trapping, continuous randomization would place an extraordinary burden on the luminescent quantum yield of the lumophore and reflectivity of all surfaces. This logic also applies to highly scattering lumophores such as nanorod agglomerates and is the reason that agglomeration is detrimental to device performance.

2.4: CdSe/CdS Core/Shell Particles

While the previous section demonstrated that the absorption spectrum tuning available in CdSe/CdS heterostructures actually results in longer photon propagation in built LSC devices, the photoluminescence quantum yield (PLQY) was too low to be truly useful. A different kind of heterostructure that maintains the tunable absorption spectrum but results in higher PLQY was needed. Recent advances in CdSe/CdS quantum dot synthesis by Chen *et al*[40] proved to be a good starting point for this research, as they showed consistently PLQY>80% for a variety of core and shell sizes, with some reaching as high as 97%.

If the particles are grown too large, they will scatter light intensely at all wavelengths. While this was not experimentally shown in the previous section, it can be calculated. We

calculated the scattering and absorption of these core/shell quantum dots with a variety of different core and shell sizes using the electrostatic dipole approximation.[48] We used bulk values of the complex dielectric constant for CdSe and CdS, neglecting quantum confinement.[46,49–51] The results of this calculation are shown in Figure 2.16. One example spectrum showing absorption and scattering is shown in Figure 2.17. By computing the scattering and absorption, the extinction (the sum of scattering and absorption) at the luminescence wavelength is predicted. Then, the extinction at high energy is divided by this low-energy extinction to provide the figure of merit, the extinction ratio Ext_{450}/Ext_{600}. The heat maps show that there is a broad optimum from 5 to 10 nm shell thickness for small 2 nm, cores that moves slightly to thicker shells for larger 5 nm cores. Therefore, the particle size which produces the longest photon propagation distances in the LSC waveguide should be in the range of 12-22 nm total diameter. The other general feature is that smaller core sizes always result in higher extinction ratios.

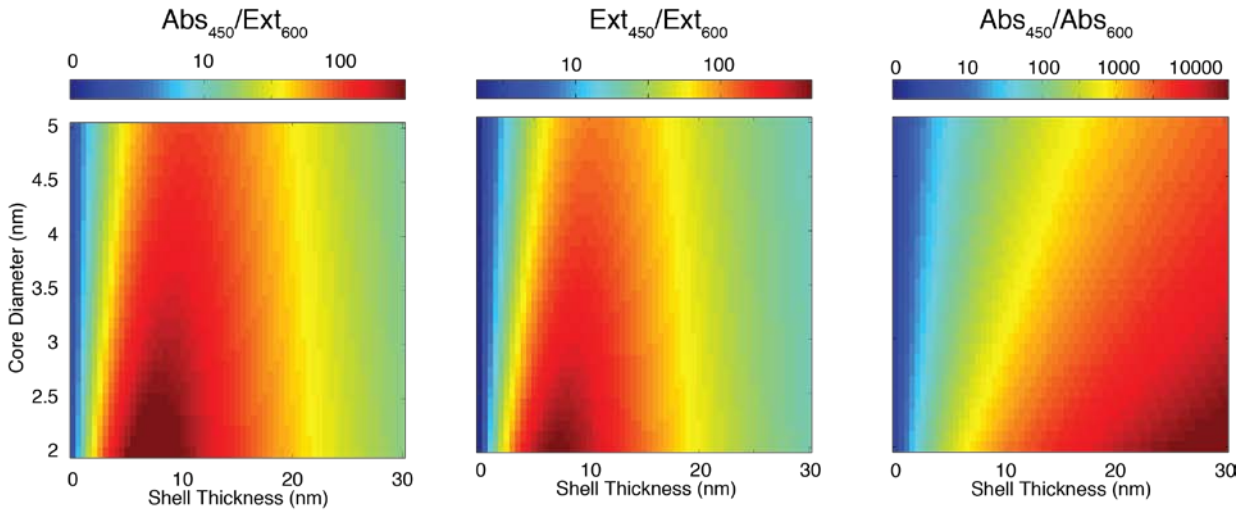

Figure 2.16: Extinction ratio calculations for a variety of core and shell sizes
From left to right, the figures show the ratio of absorption at 450 nm to extinction at 600 nm; extinction at 450 nm to extinction at 600 nm; and absorption at 450 nm to absorption at 600 nm.

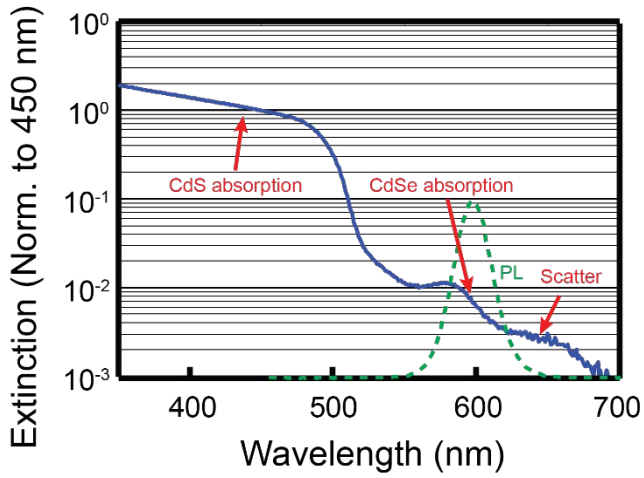

Figure 2.17: Extinction spectrum of CdSe/CdS core/shell particles
The experimentally measured extinction spectrum of CdSe/CdS core/shell particles with a 2.5 nm core and a 16 nm total diameter are shown in blue. The luminescence spectrum is shown in green.

2.4.1: Synthesis

The synthesis of these giant core/shell particles starts with CdSe seeds, just like the seeded rod synthesis, but the shelling is done differently. Instead of the fast shell growth (<5 minutes growth time) with structure-directing ligands, the shelling is done very slowly (>2 hours) with the slow addition and decomposition of less reactive precursors, and no structure-directing ligand is added. In this reaction, a constant quantity of CdSe core is used and both Cd(oleate)$_2$ and 1-octanethiol are injected slowly over the course of at least 2 hours. Thicker shells are grown by injecting at the same rate for a longer period of time, resulting in more material injected.

Synthesis of Cd(Oleate)$_2$: CdO was mixed with oleic acid at a molar ratio of 10 oleic acid per CdO and diluted to 0.2 molar in Cd with 1-octadecene. The mixture is degassed on the Schlenck line at 110 ^{o}C at 150 mTorr and complexed at 240 ^{o}C under argon. The mixture is then brought into an air-free glovebox where it can be melted and measured out by volume. The mixture is made 100 mL at a time, and typically used within a few weeks of synthesis.

CdS shelling: Quantum dot concentration was measured with the optical absorption curve provided in Jasieniak *et al*,[51] which has proven a more reliable method than the older study by Yu *et al*.[45] Then, 1e-7 moles of CdSe quantum dots are brought to 320 ^{o}C in 3 mL oleylamine and 3 mL 1-octadecene (ODE). As the mixture is being heated, injection at 3 mL per hour of 0.2 molar Cd(oleate)$_2$ in 2:1 oleic acid:ODE along with a separate solution of 0.2 molar 1-octanethiol in ODE is initiated at 250 ^{o}C with a heating rate of 20-30 ^{o}C per minute. Total injection volume sets the total shell size. After injection is complete, the solution is maintained at 320 ^{o}C for 1 hour.

Cleaning: The solution is then cooled to room temperature and cleaned in an air-free glovebox.by several successive precipitation/centrifugation/dissolution steps.

2.4.2: Characterization

To experimentally explore the extinction ratio as a function of size, 2.5 nm CdSe seeds were used to grow many different shell thicknesses. Electron micrographs of a few representative sizes are shown in Figure 2.18. Excellent size uniformity is obtained through the slow shelling technique. The faceting of the larger particles is also seen for the smaller particles when the microscope magnification is high enough, as shown in Figure 2.19.

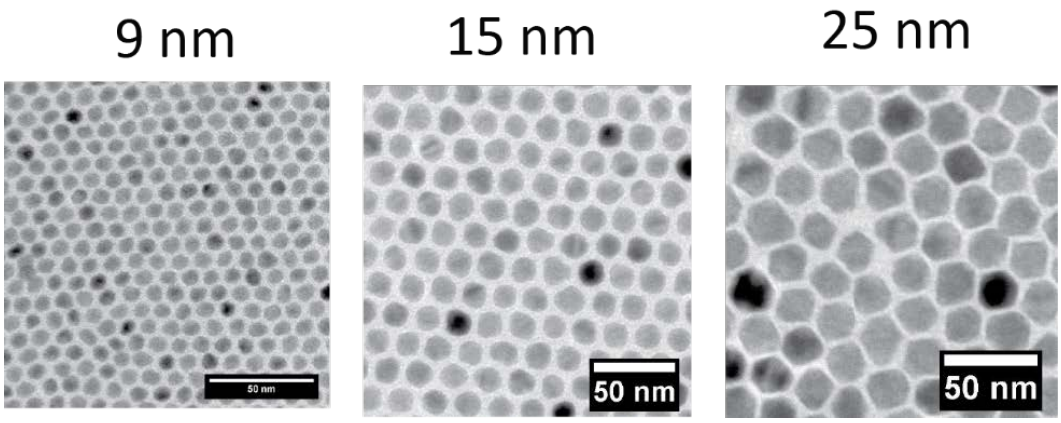

Figure 2.18: Representative TEMs of CdSe/CdS core/shell particles
Three different shell sizes are shown in this panel. The surtitle of each image is the total diameter. Scale bars are all 50 nm.

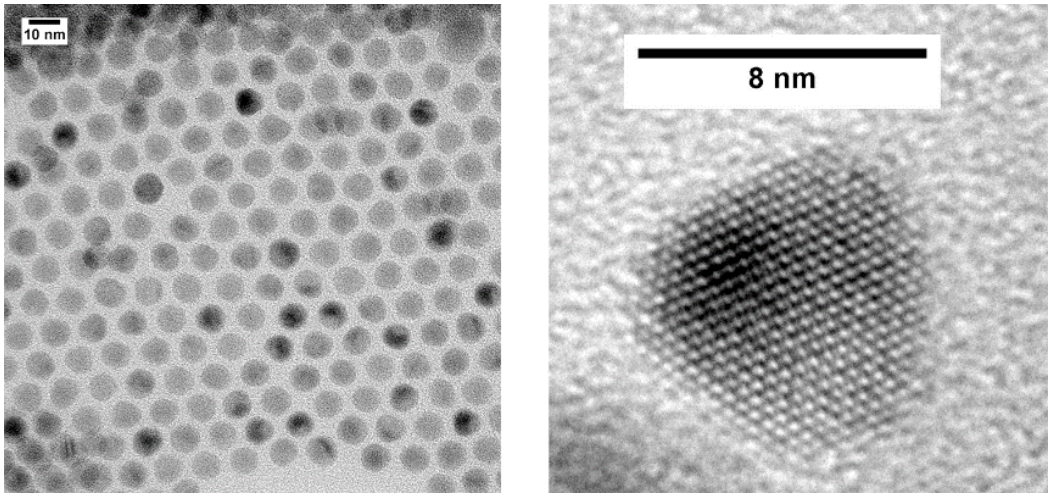

Figure 2.19: TEM micrographs showing faceting of 8 nm particles
The particles look spherical at lower magnification (left), but high magnification (right) reveals they are actually faceted. The image on the right is taken looking down the c-axis of the wurtzite structure, showing hexagonal symmetry.

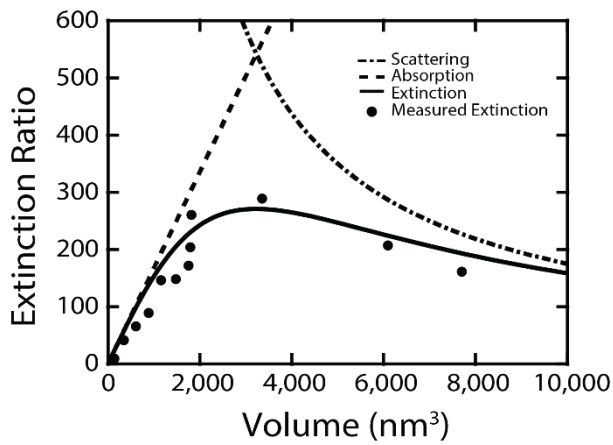

Figure 2.20: Measured extinction ratios for CdSe/CdS core/shell quantum dots
The volume is computed from transmission electron microscopy, assuming the projected area of the particles is representative of the cross section of a sphere. The two dashed lines in the graph are the ratio of extinction at 450 nm to only the absorption at 600 nm and only the scattering at 600 nm, respectively. The solid line is the computed ratio of extinction at 450 nm to the sum of absorption and scattering at 600 nm.

The extinction ratios of the size series are shown in Figure 2.20 compared to the electrostatic dipole approximation discussed above. The agreement is surprisingly good, considering that the model does not include quantum confinement.

The optimum particle based on the extinction ratio argument is found to have a 2.5 nm core and a 16 nm total diameter, yielding an extinction ratio of 230 to 1. The luminescence quantum yield of these particles was also measured, and found to be 68% in solution. This is significantly better than the giant nanorods synthesized previously, but still not high enough to make a high-performance luminescent solar concentrator.

Three changes to the synthesis resulted in huge improvements in the luminescence quantum yield. First, larger 3.5 nm cores were used (562 nm absorption exciton). Second, we removed the oleylamine which was used by Ou Chen *et al* to control the growth of the CdS shell. Third, the growth temperature was reduced from 320 °C to 310 °C. The luminescence quantum yield versus shell thickness is shown in Figure 2.21, showing that for a broad range of shell thicknesses the luminescence quantum yield can approach unity. The uncertainty in the PLQY is a result of the systematic uncertainty of the radiometric calibration lamp. The measurement technique is described in the next section.

Unfortunately, these particles seem to degrade over time. The mechanism is not known yet, but degradation from unity to around 60-80% happens over the course of months despite the particles being kept in an argon atmosphere. A solution to this difficulty would greatly improve the LSC devices made from these particles.

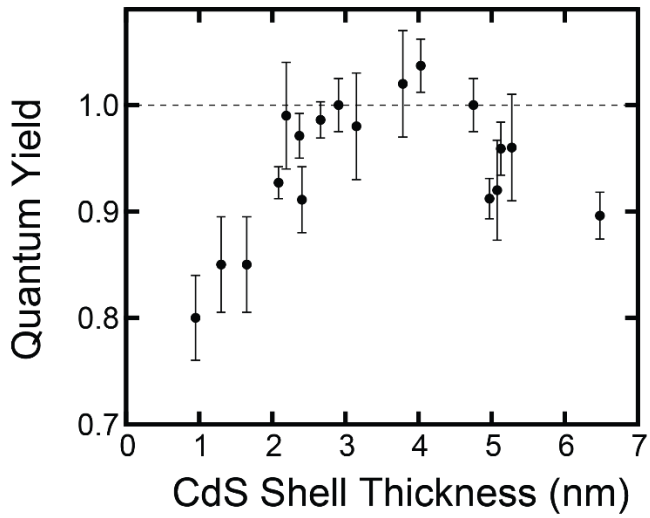

Figure 2.21: PLQY for a range of CdS shell thicknesses on 3.5 nm CdSe cores
The error bar represents the uncertainty due to the radiometric calibration source. The dashed line at unity quantum yield is the maximum credible luminescence quantum yield. Measured values can be greater than unity due to measurement uncertainty. In this case, the maximum value measured was 103%.

2.5: Measurement of Luminescence Quantum Yield

As the luminescence quantum yield approaches unity, the difficulty in measuring it accurately becomes increasingly problematic. The existing techniques all have systematic uncertainty due to the uncertainty of the radiometric calibration sources used to calibrate the spectral sensitivity of the spectrometer. The integrating sphere technique described below is the most reliable way to measure the luminescence quantum yield of semiconductor nanostructures, which often scatter a significant fraction of the incident light. Using an integrating sphere makes this irrelevant. We believe it will be important for future work to develop a highly accurate PLQY measurement, with <1% absolute uncertainty. The technique developed here has an uncertainty of 3% at best.

The technique used here is the integrating sphere technique, using a home-built integrating sphere spectrometer. A schematic of this instrument is shown in Figure 2.22. The light source is a Fianium supercontinuum laser (470-2500 nm excitation wavelength, 6 ps pulse width and 40 MHz repetition rate, 4 W output power). The integrating sphere is a 5.3” inner diameter Spectralon sphere with a 1” entrance aperture and a ¼” exit aperture. The laser is monochromated twice: first with a 150 g/mm grating in the 150 mm path length monochromator; and second with a 1200 g/mm grating in the 275 mm path length monochromator. The laser is focused onto the entrance aperture of the SP150 monochromator with a 50 mm focal length CaF2 lens, and collimated on the other end with a matched lens. The laser is then re-focused with another 50 mm CaF2 lens onto the entrance of the SP275 monochromator. After the exit from the SP275, a lens is used to focus the laser onto the entrance of the integrating sphere, after which it diverges to roughly a 2 mm x 1 cm spot at the back wall of the integrating sphere. Immediately after the final lens, a quartz beamsplitter picks off a small fraction of the beam and directs it to a ThorLabs S120VC calibrated

silicon photodiode. During operation, the photodiode monitors the laser power continuously with a 100-300 ms integration time. Both laser light and luminescence exit the integrating sphere by the ¼" port and are imaged by two CaF2 (1" diameter, 25 mm followed by 100 mm focal length) lenses onto the entrance slit of the SP2300 monochromator. This combination of lenses provides the maximum possible signal, since they capture as much luminescence from the integrating sphere as possible and project it onto all the angles the spectrograph can accept (f/4). The spectrograph is equipped with three gratings, all 300 g/mm, blazed at 500, 1000, and 1200 nm. Using a 40 um entrance slit width and accounting for the 60 um spherical aberration of the spectrometer, these gratings provide 1 nm spectral resolution (~10 nm / mm dispersion with 0.1 mm width).

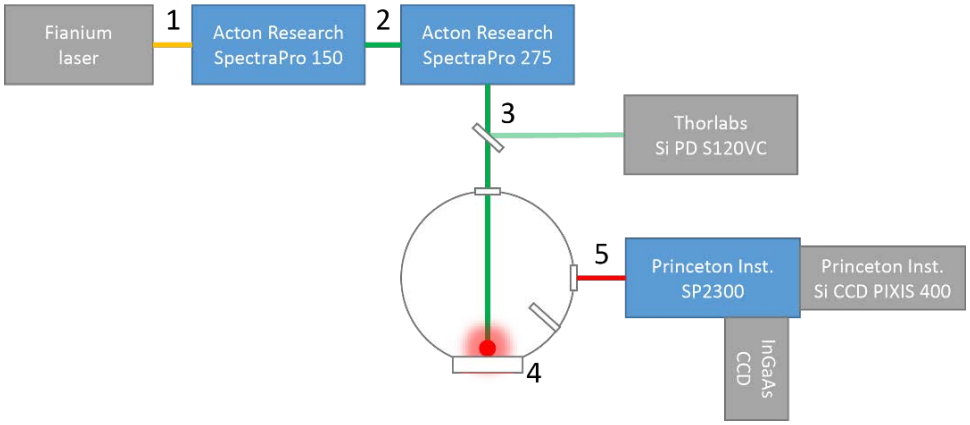

Figure 2.22: Schematic of the integrating sphere luminescence spectrometer
(1) A white light laser source is focused with lenses on entrance slit of SpectraPro150. (2) Lenses are used to focus the light onto SpectraPro275. (3) Laser beam is collimated. Beam splitter reflects ~4% onto a reference Si photodiode. Collimated laser beam enters the integrating sphere. (4) Integrating sphere with Spectralon interior coating. Sample holder places small cylindrical cuvettes with PTFE caps very near (1-3 mm) to the back wall. Baffle prevents direct out coupling of scattered, reflected, and luminesced photons. (5) Two lenses are used guide the light from the integrating sphere into the SP2300. Spectra are usually measured with the Si CCD.

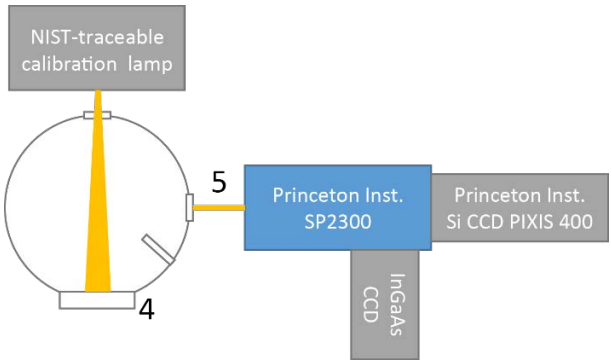

Figure 2.23: Calibration of the integrating sphere luminescence spectrometer
The NIST-traceable calibration lamp is positioned so that all of the output light couples into the integrating sphere, striking the back of the sphere near where the sample would normally sit.

There are two steps to the calibration: (1) calibrating the wavelength of the detector, and (2) calibrating the spectral sensitivity of the detector. Each of these must be done for every detector center wavelength that will be used, for both CCDs (although in practice the silicon CCD is the only one used for CdSe/CdS particles). An initial estimate of the wavelength associated with each pixel on the CCD is calculated using a diffraction grating equation. Calibrating the detector wavelength is accomplished by using a Neon gas lamp and measuring the apparent wavelength of the well-known emission peaks in its spectrum. Then, for each center wavelength, a list of pixel positions and differences between the real and measured peak positions is generated, and fit to a parabola. The parabolic fit is interpolated to provide a pixel-by-pixel correction to the wavelength. Using this technique, wavelength accuracy is found to be limited by the 0.2 nm resolution limit stemming from the 20 um pixel pitch and 10 nm / mm dispersion.

Calibration of the spectral sensitivity is more complicated. Once the wavelength calibration is complete, a NIST-traceable radiometric calibration source (in this case, OceanOptics HL-CAL-3plus) is pointed into the integrating sphere so that all the light from the lamp strikes the back of the integrating sphere where the sample holder is located. For every center wavelength, the spectrum of the lamp is measured. Dividing the known lamp spectrum S_{real} by this measured spectrum S_{meas} produces a calibration factor C for each pixel. However, there is a small amount of scattering inside the detection monochromator, which mixes all the wavelengths together a small amount. A rough estimate of the magnitude of this effect is a part in 10^4 per bin (1 nm resolution in this case) of spectral coverage. Since the calibration lamp has irradiance from 400 to the detector cutoff of 1100 nm, up to several percent of the signal at each pixel could be due to scattered light instead of true signal. This will act to raise the baseline by a constant value K.

Equation 2.7

$$C(\lambda) = \frac{S_{real}(\lambda)}{S_{meas}(\lambda)} + K$$

To measure K, the photoluminescence quantum yield (PLQY) of a standard dye is measured as a function of excitation wavelength. The value of K is varied until the measured PLQY is wavelength-independent over the ~100 nm range where the dye absorbs strongly. Rhodamine 590 dissolved in spectroscopy grade ethanol is used, and results in a PLQY of 93-96%.

The computation of PLQY, required to produce the correct value for K, must also take scattering into account. Luckily, it is easily done in this case. The method is as follows. The spectrum of the monochromated laser source is measured at a chosen center wavelength with a cuvette filled with solvent in the sample holder. The measurement is repeated for as many center wavelengths as are desired. Then the sample to be measured is placed in the sample holder, and the spectrum is measured again. Because the sample absorbs some of the laser light and emits at a different wavelength (and with a broader spectrum), the two parts of the spectrum can be mathematically separated. The blank spectrum and the sample spectrum are both corrected for the detector sensitivity by multiplication by $C(\lambda)$. The laser line is integrated in the blank spectrum S_{blank} to produce a total number of detected photons, N_{blank}. Then, the laser line is measured again with the sample spectrum S_{sample}, and integrated to produce N_{sample}. Finally, the blank

spectrum is multiplied by the fraction of laser photons that remain in the sample spectrum, and this spectrum is subtracted from the sample spectrum to produce a corrected spectrum S_{corr} which can easily be integrated over the photoluminescence wavelengths to produce the number of luminesced photons N_{PL}. Then, the ratio of luminesced photons to absorbed photons is the PLQY. Typical correction factors and the luminescence yield of rhodamine 590 and rhodamine 640 are shown in Figure 2.24 and Figure 2.25 respectively.

Equation 2.8

$$S_{sample} = S_{sample,meas} * C$$

Equation 2.9

$$S_{blank} = S_{blank,meas} * C$$

Equation 2.10

$$N_{blank} = \int_{laser} S_{blank} d\lambda$$

Equation 2.11

$$N_{sample} = \int_{laser} S_{sample} d\lambda$$

Equation 2.12

$$S_{corr} = S_{sample} - \left(\frac{N_{sample}}{N_{blank}}\right) S_{blank}$$

Equation 2.13

$$N_{PL} = \int_{PL} S_{corr} d\lambda$$

Equation 2.14

$$PLQY = \frac{N_{PL}}{N_{blank} - N_{sample}}$$

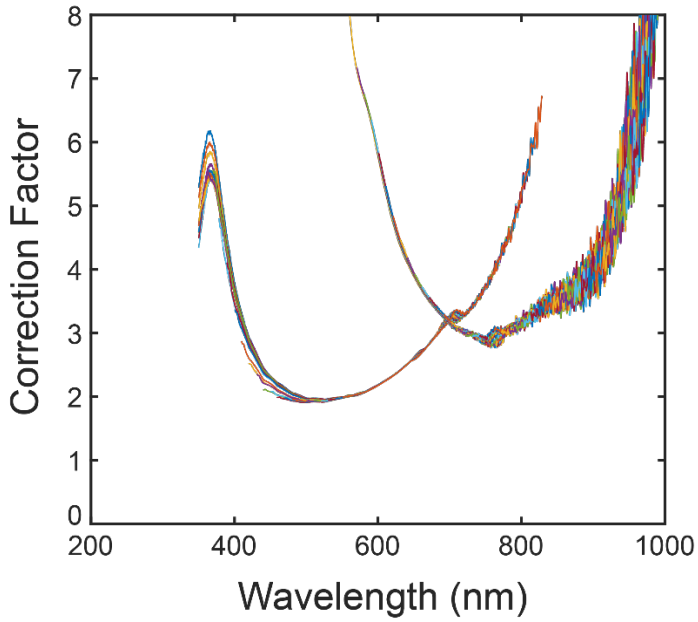

Figure 2.24: Spectral sensitivity of the integrating sphere luminescence spectrometer
Two different gratings are used, having a 500 nm blaze angle and a 1000 nm blaze angle, which each produce a family of nearly overlapping curves for different detector center wavelengths. Each family of curves contains dozens of correction spectra for different center wavelengths, each plotted in a different color. The spread of the different spectra at a given detection wavelength is due to the etalon of the detector: anti-reflection coatings make the detector have a wavelength- and angle- dependent sensitivity. Different center wavelengths result in the same wavelength hitting the camera at different angles, resulting in different correction factors.

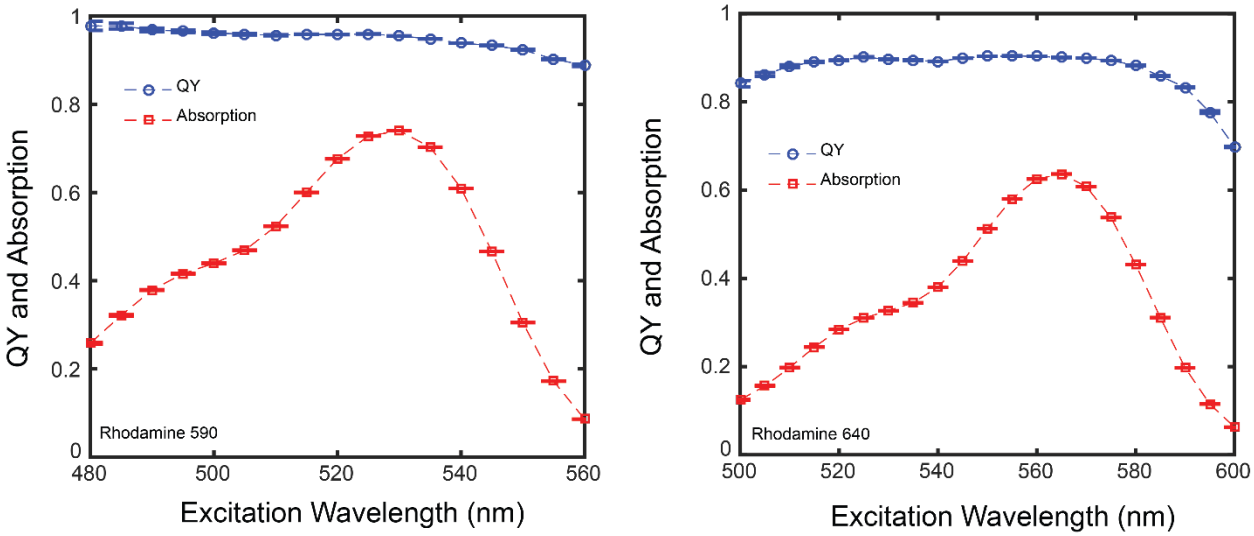

Figure 2.25: Calibrated PLQY measurement of rhodamine 590 and 640
The luminescence quantum yield is mostly wavelength-insensitive once the correct K is chosen. The error bars represent the measurement repeatability. The systematic error of 3% relative is not included here, but still applies. The average measured QY of Rhodamine 590 is 95%, and the average measured QY of Rhodamine 640 is 89%.

Chapter 3 : Optical Design

The design of a luminescent solar concentrator requires more than simply choosing the right lumophore with the right absorption spectrum. The considerations described in Chapter 2 fall short of making a high performing device because at best, only the photons captured by total internal reflection (TIR) can be used by the LSC, which amounts to 70-80% for most polymers.

This chapter will describe the optical design of LSCs, describing geometric considerations, thermodynamic principles, and the photonic design required to achieve high performance.

3.1: Desired Absorption Spectrum

The desired absorption spectrum for the perfect LSC lumophore, described in Figure 2.1, still leaves some room for improvement. The fundamental mantra of any new photovoltaic power conversion device is "a good solar cell is a good LED." That is, a perfect solar cell exhibits a sharp luminescence at its band edge, with external radiative efficiency (ERE) approaching unity.[27,52] The energy and intensity of the luminescence from a solar cell determines the voltage under illumination. In the case of the luminescent solar concentrator, the ideal material to produce intense low energy (E_2) luminescence from a high energy (E_1) absorption band does not produce the correct absorption spectrum to make the LSC produce high voltage. If the material is designed to emit at the higher energy E_1, then it is not acting as a luminescent solar concentrator. But if the material emits from the lower energy state (E_2), then the voltage will be lower than desired for a material that absorbs primarily at the higher energy E_1.

This conundrum is intrinsic. Fortunately, a solution is at hand. A spectrally selective filter should be used to decouple the low energy luminescence from the rest of the universe. This idea has been proposed by many scholars over the years, but the practical realization has been fleeting. In fact, it has previously been shown that a wavelength-selective dielectric filter is thermodynamically required to achieve high efficiency.[53] Under idealized circumstances where the lumophore species has unity quantum yield, the polymer-lumophore matrix exhibits no scattering over the length-scale of the concentrator, and the Stokes shift is large enough to allow for a high thermodynamic limit for *C*, the performance of the LSC will still be limited by inefficient light guiding to the solar cell. In the traditional LSC design, the waveguide acts as a rudimentary wavelength-selective filter for photons: high energy solar photons are refracted to subtend only a fraction of the solid angle inside the waveguide, whereas low energy luminesced photons exist at all angles and accumulate inside the totally internally reflected modes.[54] The wavelength-selectivity of this filter is inherently poor due to escape cone losses, and can be improved with the addition of a wavelength-selective photonic mirror between the waveguide and the sun. Several scholars have made experimental attempts at this over the last several years, showing modest improvements in the concentration factor and collection efficiency.[10,14,19,36]

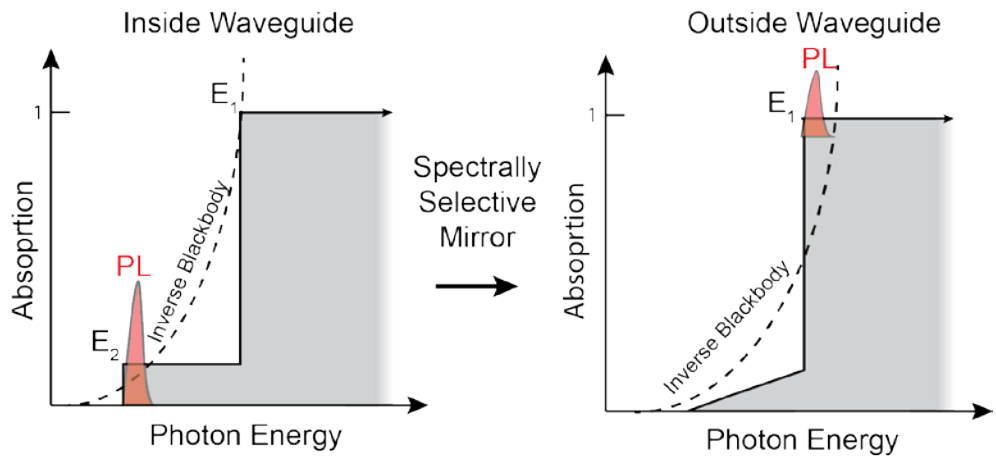

Figure 3.1: Desired absorption spectrum of the LSC
Inside the LSC, the absorption spectrum must allow low energy luminescence. The LSC device, as a whole, must appear to the universe as the schematic on the right, only allowing high energy luminescence.

In reality, all LSCs in existence today are limited by photon transport. The scaling laws described in Chapter 1 between Stokes shift and concentration factor are never achieved in practice. It is instructive to consider that the dominant loss mechanism of luminescent solar concentrators is incomplete trapping of luminescence. The scaling laws that are actually in effect in these real devices are described in Figure 3.2. The geometric gain G of the device is defined to be the ratio of the top area to the edge area of the waveguide, and for most practical waveguide shapes (e.g. circles and squares) this ratio is the waveguide length divided by four times the thickness.

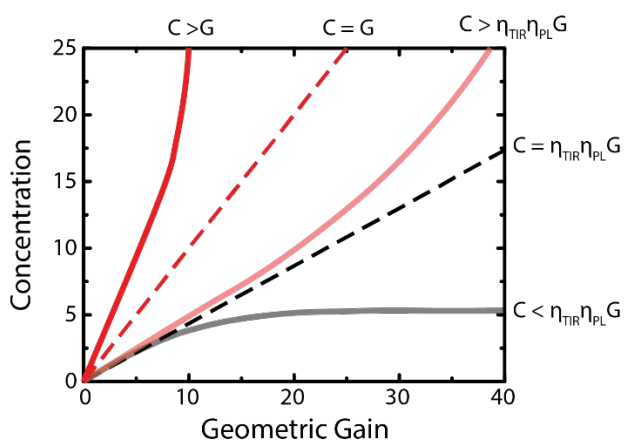

Figure 3.2: Scaling laws in transport-limited LSCs
The different regimes for photon transport in LSCs is shown schematically. Poorly performing LSCs exist below the dashed black line. Extremely high performing LSCs exist above the dashed red line. Between the two dashed lines, either poor luminescence quantum yield or poor luminescence trapping is hindering device performance.

Most LSCs in literature have relied on total internal reflection (TIR) to trap photons, resulting in concentration factors of that scale linearly with the geometric gain, with a slope limited by the quantum yield and the fraction of photons trapped by TIR:

Equation 3.1

$$C \leq G\, \eta_{TIR}\, \eta_{PL}$$

Improving the luminescence quantum yield and the fraction of photons trapped by TIR do increase the slope of this limit, but do not result in devices that approach the thermodynamic limits of either concentration factor or power conversion. Improving the trapping efficiency for photons dramatically past the 70%-80% normally achieved by TIR can result in a super-linear relationship between C and G, as photon diffusion starts to play a role. In the limit of extreme light trapping and unity quantum yields, with solar cells on the edge of the waveguide that do not have appreciable ERE themselves, the limit of C=G is reached. Allowing these solar cells to luminesce efficiently, C>G can be achieved, and the device is no longer limited by photon transport. In that case, the thermodynamic approach is more appropriate than these transport considerations, and the methods of Chapter 1 are more useful.

3.2: Simulations

In reality, even a LSC designed in accordance with the optical principle of Figure 3.1 will not perform at the thermodynamic limit, because small loss mechanisms like parasitic absorption and material defects will always be present. It is of utmost importance to understand how these defects impact the device performance. Bridging the gap between the transport-limited LSCs and the thermodynamically limited LSCs requires accurate simulations. Since existing luminescent solar concentrators are all limited by photon transport in the waveguide, these simulations focus on photon transport. These simulations must be able to produce the thermodynamic limits when perfect material parameters are used; they must faithfully reproduce the behavior of poorly operating devices; and hopefully, they can chart a path between those two regimes.

3.2.1: Monte-Carlo Simulation

Monte-Carlo ray-tracing simulations have been used to model the performance of luminescent solar concentrators by many scholars. In general, they are highly accurate and can model a wide variety of LSC shapes, sizes, and designs.[18,23,32,35,55–57]

For this study, Monte-Carlo ray-tracing simulations are performed by collecting statistics on large numbers of photons incident on the LSC. The logic flow of the simulation is shown in Figure 3.3. A photon is created immediately above the LSC sheet, moving directly downward into the sheet. The photon is moved forward 5 μm, and then a series of checks are performed. The photon can be absorbed or scattered, and at every interface it can reflect or refract. Absorbed photons can be luminesced, or they can be lost to nonradiative events. Luminescence, scattering, and reflection are all treated probabilistically with a random number generator initiated to the computer epoch. Since both absorption probability in the silicon and refraction/reflection coefficients are polarization-dependent, the polarization of the photon is maintained until a scattering or luminescence event allows it to randomize. Photons are created at every point in a

rectangular grid with 50 μm spacing. Additionally, every grid-point is populated with photons spanning 320 nm to 1100 nm at 10 nm increments. After the simulation is complete, each photon is weighted by its relative solar intensity to simulate a solar spectrum.

Reflection and refraction coefficients are calculated with Fresnel coefficients, assuming the refractive index of the glass is 1.5 and the PLMA is 1.4 at all wavelengths. Additionally, the absorption probability of each photon in the thin silicon photovoltaic cell is calculated with the finite-difference time-domain method (FDTD) using Lumerical® FDTD Solutions© 8.6, with optical constants taken from the SOPRA database built into the program. The 2-dimensional FDTD simulation is performed from 0 to 85 degrees in 5 degree increments, and from 320 to 1100 nm in 10 nm increments. A periodic boundary condition is used. The geometry is a 30 μm thick piece of silicon with a background index of 1.4, which accounts for the silicon being embedded in PLMA on the sides with quartz on the bottom and an amorphous SiO_2 passivation layer on the top.

The absorption probability at each step is calculated from the absorption spectrum of the nanorods and the measured optical density of the films**.** Since absorption in both the nanorods and the photovoltaic cell is strongly wavelength dependent, wavelength is maintained until a luminescence event randomizes it. Every luminescence event creates a new wavelength with probabilistic weighting such that the measured luminescent spectrum of the nanorods is reproduced.

Every photon absorbed in the silicon photovoltaic is assumed to be collected as current. The photocurrent as a function of aperture radius is calculated by calculating the radius of every grid point and integrating only the photons with a radius less than or equal to the simulated radius. By this method, one large simulation can simulate every radius smaller than the illuminated spot size.

The simulations generally involve between 10^7 and 10^9 photons. Each photon requires many random number generation computations, making the simulation very computationally expensive. While the simulation was originally written in MATLAB, this proved too slow to collect enough statistics. To enhance the speed of the simulation, the MATLAB parallelization toolbox was used to parallelize the simulation to 12 cores on a 16-core workstation. Additionally, the code was compiled into C-code using the MATLAB Coder package, which allows the C-code to be executed from within the MATLAB parallel for-loop. The combination of these two speed enhancements (12-fold speed-up for the parallelization and 100-fold from C-compilation) allowed the simulations to be completed in a timely manner.

The results of this simulation are compared to experimental data in FIG X. The agreement is very good in this low performance regime.

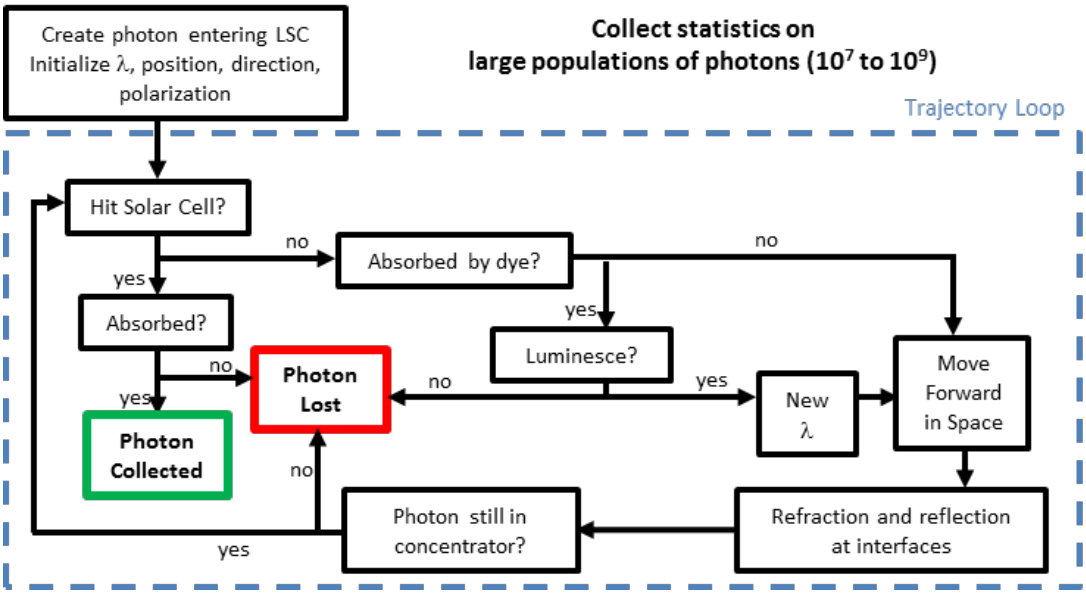

Figure 3.3: Control flow of the Monte-Carlo LSC simulation

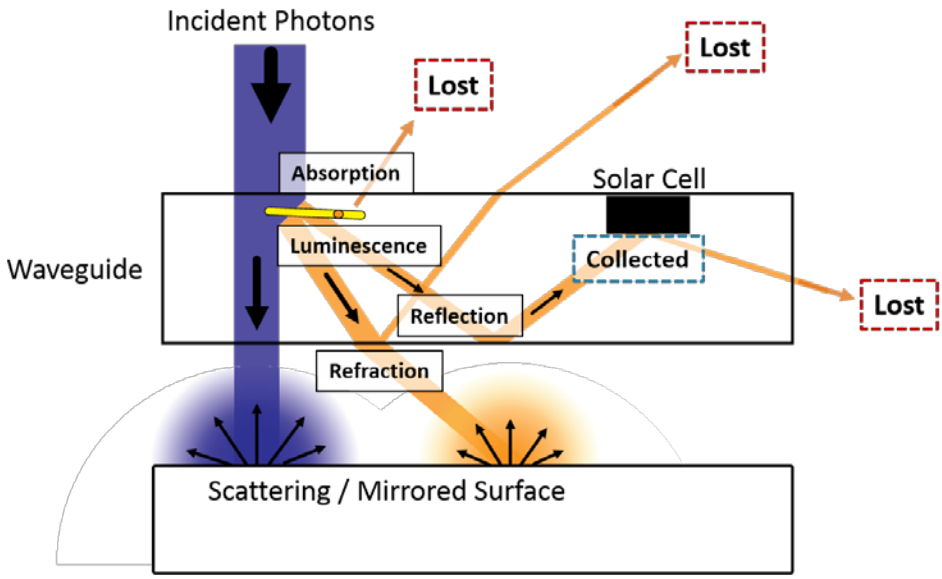

Figure 3.4: Paths and processes in the Monte-Carlo simulation
The streams of photons are shown as colorful lines. Some representative probabilistic paths shown. Blue photons are incident high energy photons, and they are converted to orange photons by the nanorod.

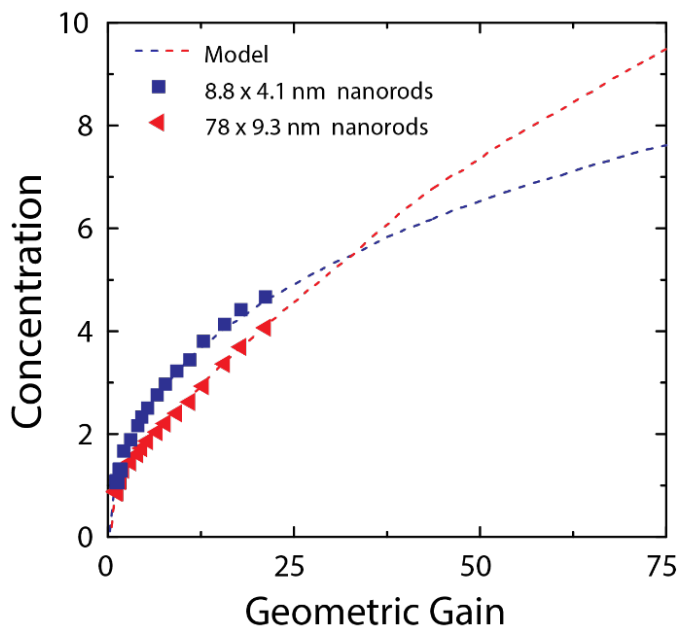

Figure 3.5: Comparison of Monte-Carlo simulation to experiment
The experimental data are taken from the nanorod LSC devices, which suffered from low optical absorption at high energy, low luminescence quantum yield (70% for the 8x4 nm nanorods and 35% for the 78x9 nm nanorods), and only a 72% TIR efficiency. Regardless, the agreement between the experiment and the simulation is excellent.

3.2.2: Generalized Finite Element Photon Transport Model

While the Monte-Carlo method is accurate, it is extremely computationally expensive. Additionally, each small change to the device requires running a new simulation. As a result, it is difficult to extract general design principles from it.

A different method entirely is to solve the Beer-Lambert Law in a multimode waveguide with non-dimensional units used for the absorption, Stokes shift, PLQY, geometric gain, and reflectivity for non-TIR angles. While the photon transport equations can be written down with relative ease, solving them analytically is difficult. An iterative numerical solution using finite-element modeling is straightforward, and can be solved rapidly (seconds) on a modern computer.

This model uses the following definitions:

$QY \equiv$ Luminescent Quantum Yield

$i \equiv$ Loop iteration

$\alpha \equiv$ Absorption at high energy

$R \equiv$ Reflectivity of mirror

$S \equiv$ Ratio of absorption at high energy to low energy

$\phi \equiv$ Zenith angle

$r \equiv$ Lateral distance from luminescent point

$I \equiv$ Luminescence intensity

Each luminescence event results in isotropic emission. Therefore, the luminescence at one point in the waveguide results in an absorption profile throughout the waveguide according to the following equation, which considers the angular spread of photons, the reflectivity of the waveguide interface as a function of angle, and the absorption coefficient of the lumophore.

Equation 3.2

$$A_{i,x,y} = \sum_{x,y} \int_{\phi=0}^{\pi/2} I_{i,x,y} \frac{\alpha}{2\pi r S} \exp\left(-\frac{\alpha}{S * r * \sin\phi} + \frac{\log R(\phi) \tan\phi}{r(x,y)}\right) \sin\phi d\phi$$

Escape of luminesced photons is calculated similarly:

Equation 3.3

$$E_{i,x,y} = \int_{\phi=0}^{\pi/2} -\frac{I_{i,x,y} \log R \tan\phi}{2\pi r} \exp\left(-\frac{\alpha}{S * r * \sin\phi} + \frac{\log R(\phi) \tan\phi}{r(x,y)}\right) \sin\phi \, d\phi$$

Luminescence is calculated from the absorbed flux and the luminescence quantum yield:

Equation 3.4

$$I_{i+1,x,y} = \sum_{x,y} A_{i,x,y} * QY$$

Collection of photons is calculated to be all the non-absorbed, non-escaped photons:

Equation 3.5

$$Collection_i = 1 - \sum_{x,y} E_{i,x,y} - \sum_{x,y} A_{i,x,y}$$

Equation 3.6

$$\eta_{coll} = \sum_i Collection_i$$

Equation 3.7

$$Survival = Mean\left(I_{i,x,y}\right)$$

In order to compute the behavior of the entire film, a single computed matrix of the absorption and escape profiles is rastered across the waveguide according to Figure 3.6.

The starting luminescence population is assumed to be constant across the waveguide: $I_{0,x,y} = 1$. For each iteration i and each grid point x, y and each zenith angle ϕ the following values

are calculated according to Equations (1)-(6). When the survival of photons decreases below a target threshold of 1E-4, the calculation is terminated.

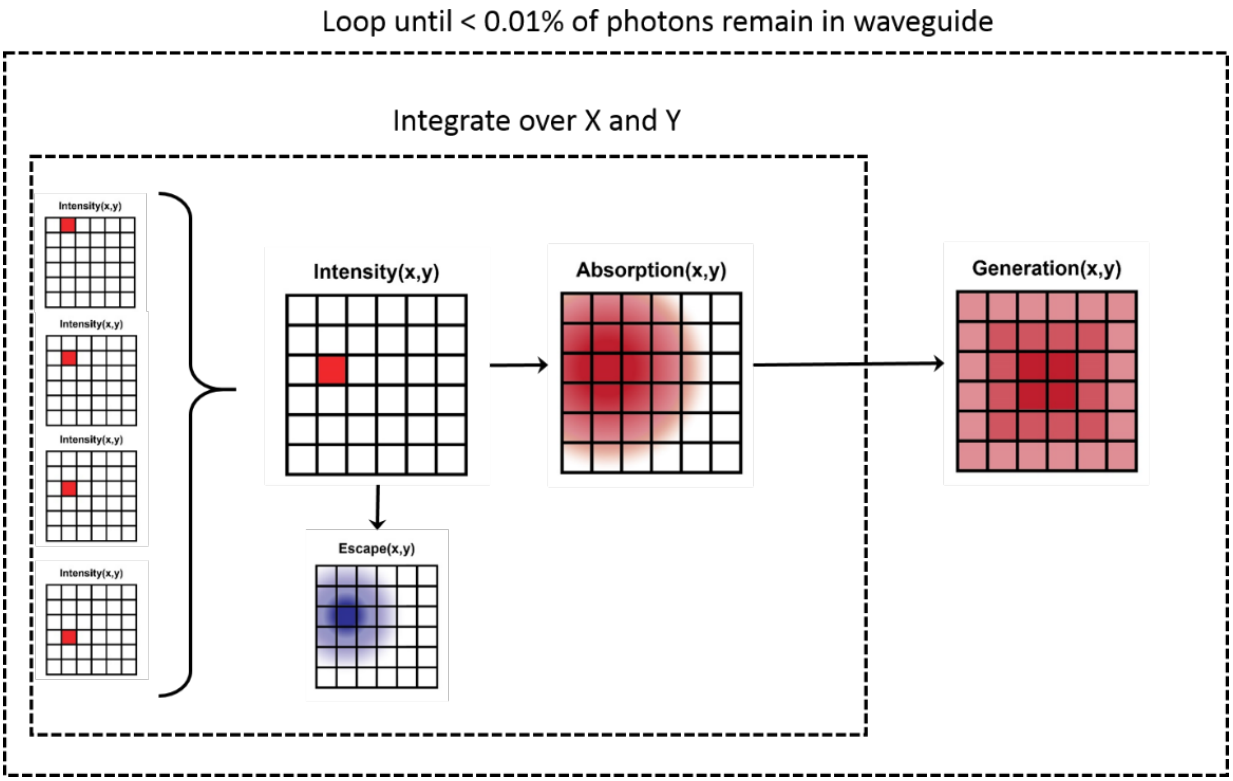

Figure 3.6: Finite-element Beer-Lambert solver
The luminescence intensity at each point in the waveguide is used to generate a new absorption and escape profile. Rastering across the waveguide and summing yields a new generation profile, which is fed back into the next iteration of the computation. After each loop cycle, the collected photons are set equal to the number of photons that were neither reabsorbed nor escaped.

Some of the results of this computation can be found in Figure 3.7, showing the effect of non-unity reflectance, reabsorption by the lumophore, and varying geometric gain of the waveguide. The figure shows that at low loadings of dye, increasing the dye loading allows more photons to be absorbed, and therefore increases the concentration factor. As more dye is loaded into the waveguide, at some point the dye starts to reabsorb the luminesced photons. Even if the dye has a very high luminescence quantum yield (assumed to be 99% in this computation), a large fraction of the luminescence couples to the escape cone. Therefore, the waveguide efficiency starts to drop, and eventually the concentration factor decreases as well. This problem can be mitigated by trapping the luminesced photons with spectrally selective reflectors. In order to achieve waveguide efficiency >90% with geometric gain of 100, a reflectivity exceeding 99% is required.

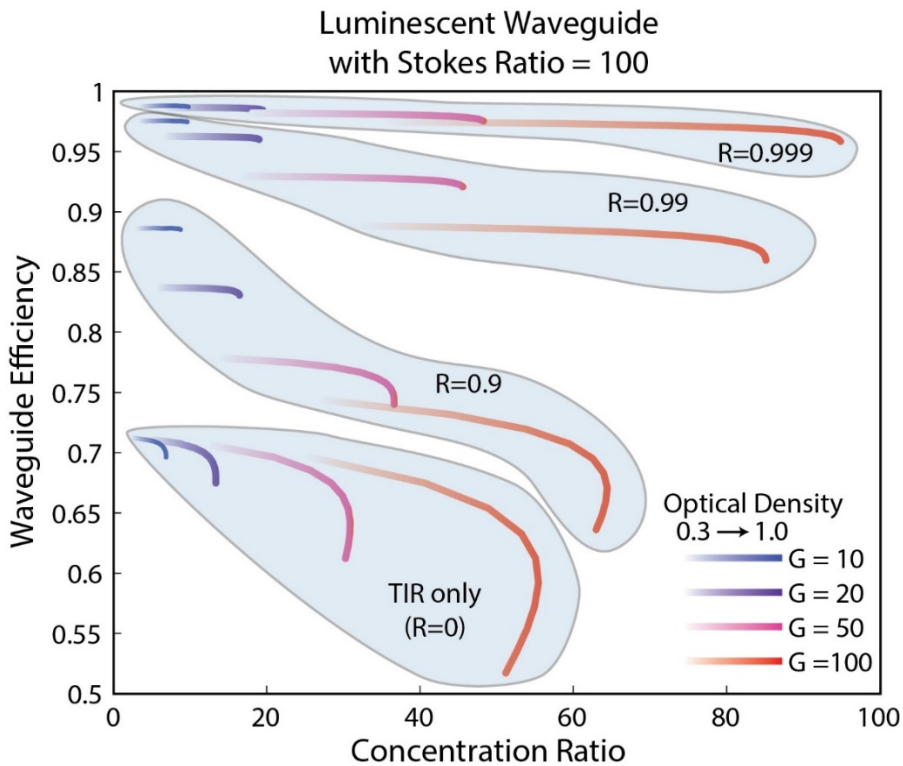

Figure 3.7: Generalized LSC performance modeling
Each family of curves represents a different reflectivity of the LSC, assuming TIR angles have unity reflectivity. The plot shows the waveguide efficiency (fraction of absorbed photons that reach the waveguide edge) versus the concentration ratio, which is the product of the fraction of incident photons absorbed and the waveguide efficiency. Within each family, each curve represents a different geometric gain. Traversing left to right along each curve increases the lumophore loading. The lumophore is assumed to have a Stokes Ratio of 100 and a luminescence quantum yield of 99% in this calculation.

3.3: Dielectric Multilayers

Typically, omnidirectional reflection is associated with only metals and 3-d photonic crystals.[58,59] Metals are lossy and do not have sufficient spectral selectivity for our purpose. And unfortunately, 3-d photonic crystals operating in the visible are unavailable due to the requirement for high refractive index ($\epsilon' > 12$) and low loss ($\epsilon'' \approx 0$).[60,61] Therefore, a different solution is needed.

Periodic dielectric stacks can function as omnidirectional reflectors. The exact design rules for a dielectric stack with a single periodicity were solved in 1998 by Winn *et al*.[62,63] A semi-infinite stack of dielectric layers with quarter-wave thickness for a target wavelength can be made, where the two different materials used have different refractive indices n_1 and n_2 and thicknesses d_1 and d_2 such that $n_1 d_1 + n_2 d_2 = \frac{\lambda}{2}$. In general, the best results are found for structures resembling a quarter-wave stack: $n_1 d_1 \approx n_2 d_2 \approx \frac{\lambda}{4}$. While such a 1-d photonic crystal does not have a complete photonic band-gap, it can have omnidirectional reflection due to the low refractive

index of the surrounding medium (usually air). In this case, photon modes inside the reflection band do not overlap with photon modes in the medium, and thus omnidirectional reflection is achieved. The graphical representation of this condition can be seen in Figure 3.8. The numerical criteria for this stop-band are:

Equation 3.8

$$0 < \frac{\Delta\omega}{2c} = \frac{a\cos\left(-\frac{\sqrt{A-2}}{\sqrt{A+2}}\right)}{n_1 d_1 + n_2 d_2} - \frac{a\cos\left(-\frac{\sqrt{B-2}}{\sqrt{B+2}}\right)}{d_1\sqrt{n_1^2-1} + d_2\sqrt{n_2^2-1}}$$

Equation 3.9

$$A = \frac{n_2}{n_1} + \frac{n_1}{n_2}$$

Equation 3.10

$$B = \frac{n_2\sqrt{n_1^2-1}}{n_1\sqrt{n_2^2-1}} + \frac{n_1\sqrt{n_2^2-1}}{n_2\sqrt{n_1^2-1}}$$

where $\Delta\omega$ is the bandwidth in frequency, $a = d_1 + d_2$, and c is the speed of light in a vacuum. The results of this computation are shown in Figure 3.9.

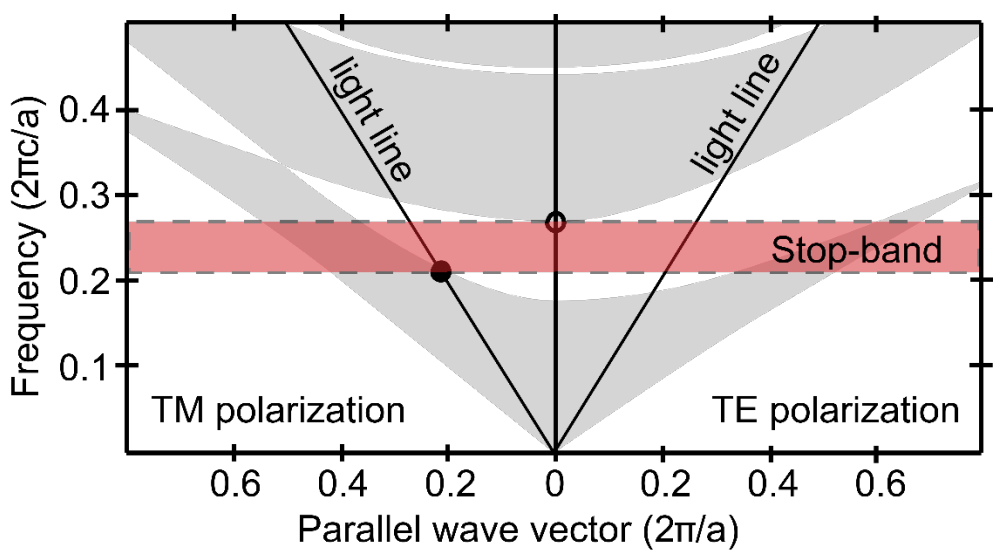

Figure 3.8: 1-d photonic crystal omnidirectional reflector
The photonic band structure of the photonic crystal for omnidirectional reflection are shown, with n_1=1.7 and n_2 = 3.4. The grey zones contain photon modes in the crystal, and the light line is shown for comparison. The open circle is the maximum frequency of the stop band, and the filled circle is the lower frequency of the stop band, which is highlighted in red. If the refractive indices n_1 and n_2 are sufficiently high, as in this case, the band structure is stretched horizontally but the light line is unchanged, resulting in an omnidirectional stop-band. Adapted from Reference 62.

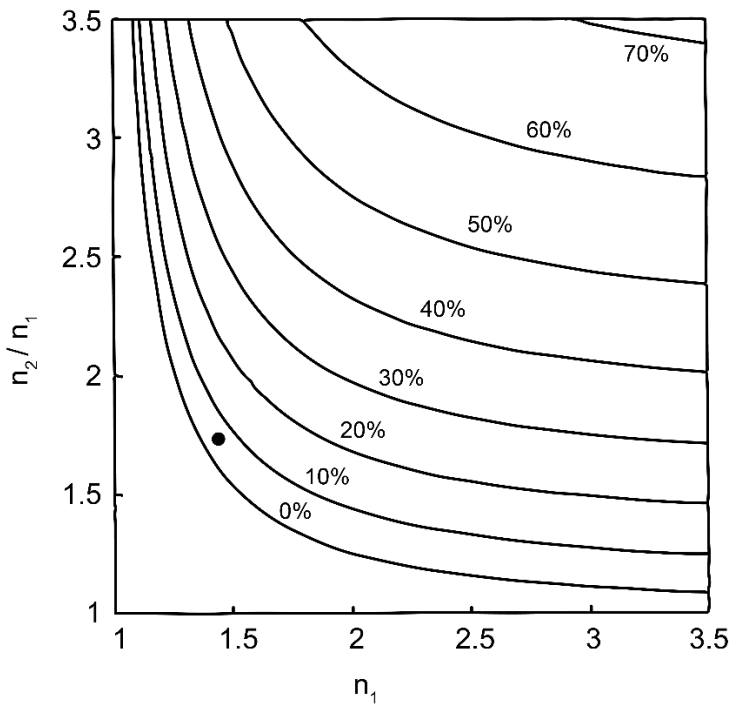

Figure 3.9: Bandwidth of omnidirectional 1-d reflector
The reflection width contours are plotted for a variety of refractive index pairs (n_1 and n_2), with air on both sides of the stack. The contour lines are labeled by the percentage of the center frequency contained in the stop band (range to mid-range ratio). The black dot represents the pair of materials used in our model, ZnS and SiO_2. Adapted from Reference 63.

The criteria for omnidirectional reflection of incident rays, then, is directly related to the refractive index of the dielectric materials available for the mirror. Photons impinging on the mirror from a lower index medium (like air) will refract toward the normal due to the high index of the dielectric materials. Therefore, these photons only occupy the escape cone once inside the mirror, as depicted in Figure 3.10. If there are no photon modes in the escape cone inside the dielectric quarter-wave stack, then these photons can only exist as evanescent waves inside the mirror and will be reflected completely (so long as the dielectric material is not too lossy). The design even works if there is no air-gap between the luminescent waveguide and the dielectric mirror, so long as the front surface of the glass support is sufficiently smooth to allow for efficient total-internal-reflection. Without the air between the luminescent waveguide and the dielectric mirror, the photons from the waveguide can travel into the glass and be reflected by the total-internal-reflection on the front surface of the glass (since all photons in the escape cone were reflected by the mirror). The backside reflector can be anything with high reflectivity toward the luminesced photons, like a dielectric-metal mirror, or a white scattering material.

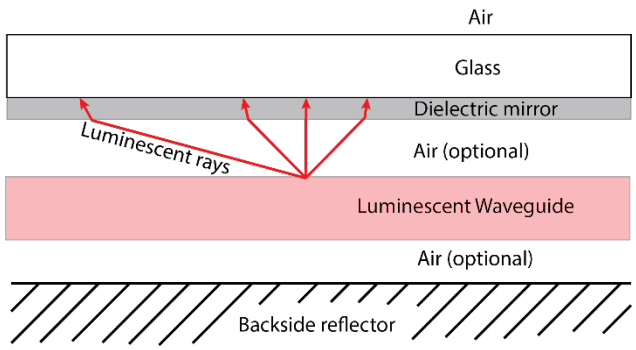

Figure 3.10: Device stack using dielectric omnidirectional reflector
Photons, shown as red rays, impinging on the mirror from a low index medium like air refract toward normal angles, and can only refract into escape-cone angles.

The difficulty, then, is to find two dielectric materials that satisfy the requirement of Equation 3.8 and Figure 3.9. It turns out that ZnS (zincblende) and SiO2 meet the criteria, and their combination is plotted as the black dot in Figure 3.9. The predicted range/midrange ratio for this pair of materials is 7%, resulting in a bandwidth of 140 meV for a 2 eV center frequency. This is wide enough to reject a majority of luminescence from quantum dots, which have a single-particle width of around 60-90 meV.[64,65]

We designed a simple Bragg stack using a T-matrix method built into Lumerical® FDTD Solutions 8.6.2 (the stackrt function). This allowed us to account for both the refractive index and the loss of the model materials. The two alternating materials used were SiO_2 and ZnS, with complex refractive index data taken from the SOPRA database. The reflection coefficient of a photon passing from a material of index 1.4 through stacks of varying numbers of layers and varying thicknesses and into the air (index 1) were calculated for 200 to 1100 nm (1 nm increment) and 0 to 90 degrees (1 degree increment) for both S and P polarizations. The reflectivity was averaged over wavelength, weighted by the emission spectrum of a typical nanorod and a constant brightness hemisphere ($2 \sin\theta \cos\theta \, d\theta$).

A typical nanorod emission spectrum, for luminescence escaping a polymer film, is plotted against the computed reflectance spectrum at normal incidence and 44 degrees in Figure 3.10. The critical angle in the medium is 45 degrees, after which all wavelengths are reflected well. The angle-averaged reflectance for a typical nanorod emission spectrum as a function of layer thickness is shown in Figure 3.11. The simulated reflectivity spectrum was used in Monte-Carlo simulations to predict device performance.

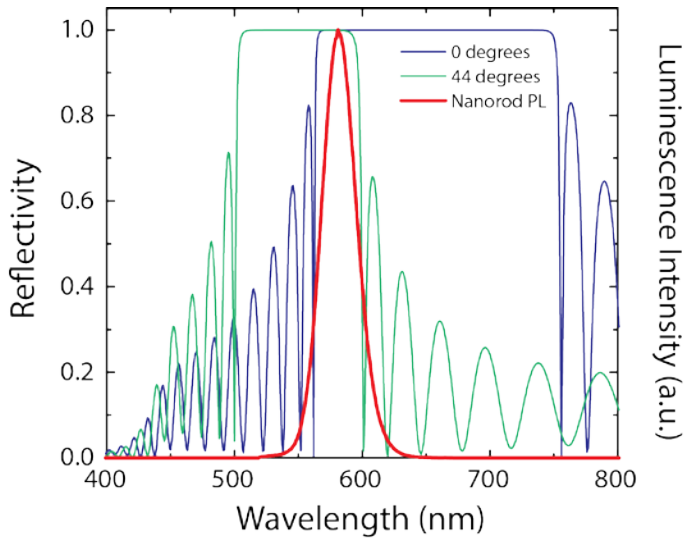

Figure 3.11: Reflectance of a Bragg mirror versus PL of nanorods
The luminescence spectrum of a sample of CdSe/CdS nanorods is shown in red, with the calculated reflectance of a SiO_2/ZnS quarter-wave stack shown in blue and green. The green line is for the TM polarization at the very edge of the escape cone, 44 degrees. TE polarization is more easily reflected. Therefore, a calculated omnidirectional reflection of 0.15 eV on the 2.1 eV center frequency. The 7% computed range/midrange ratio matches the predicted bandwidth for this pair of materials very well.

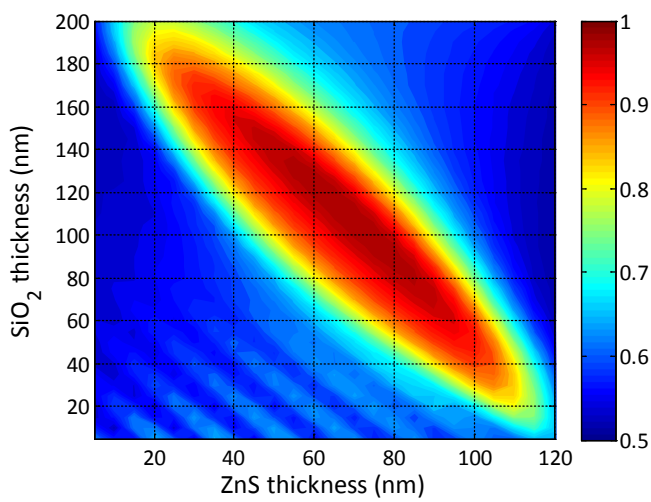

Figure 3.12: Layer thickness dependence of Bragg mirror reflectance
The angle- and wavelength- averaged reflectance of the Bragg mirrors are plotted for a variety of different layer thicknesses. The optimum is around 99.5% for 70 nm ZnS thickness and 110 nm SiO_2 thickness.

In the Monte-Carlo simulation, a periodic boundary condition was applied to simulate the devices in the limit of a very long waveguide. Figure 3.12 shows the effect of nanorod size on the concentration factor for a range of luminescent quantum yields. Holding the quantum yield constant shows that, in the regime of excellent light trapping, there is a nearly linear relationship between nanorod volume and photon concentration factor. This is due to the reduced reabsorption

of the larger nanorods: linear increases in volume result in linear increases in the propagation length of photons inside the LSC, resulting in more chances for the photon to be absorbed by the solar cell. As the nanorod volume gets very large, the propagation distance asymptotes due to scattering in the polymer matrix. While the simulations did not include the effects of scattering by the nanorods, this is found to be a small effect for the sizes of nanorods used in this study. Further increases in the nanorod volume would likely cause the scattering to overwhelm the reduced reabsorption of the larger rods and result in diminished concentration factors.

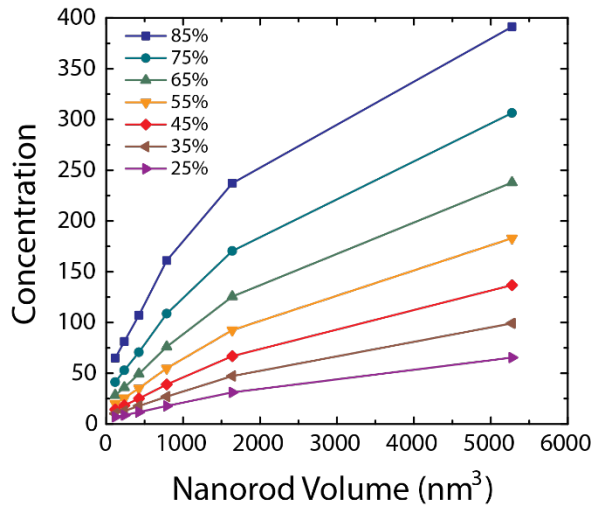

Figure 3.13: Simulated LSC devices with simulated mirrors
Each curve is a series of LSC device simulations for a size-series of nanorods, utilizing optimized Bragg mirrors for each size of nanorod, holding the PLQY constant at the value indicated in the legend.

3.4: Performance in Devices

The Monte-Carlo simulation indicates that concentration factors exceeding 100 should be attainable with dielectric stack mirrors. A custom dielectric mirror was fabricated by a custom optics company, Optical Filter Source LLC (Austin, Texas). The reflectance spectrum was measured in transmittance mode in a Shimadzu UV-3600 double-beam absorption spectrometer. The mirror was glued to a post and rotated to different angles from 0 to 85 degrees, without a polarizer. The results are plotted in Figure 3.13. The hemispherically-averaged spectrum is shown in Figure 3.14.

Core/shell particles shown in the middle panel of Figure 2.18 were used to make devices. Their absorption spectrum is shown in Figure 2.17.

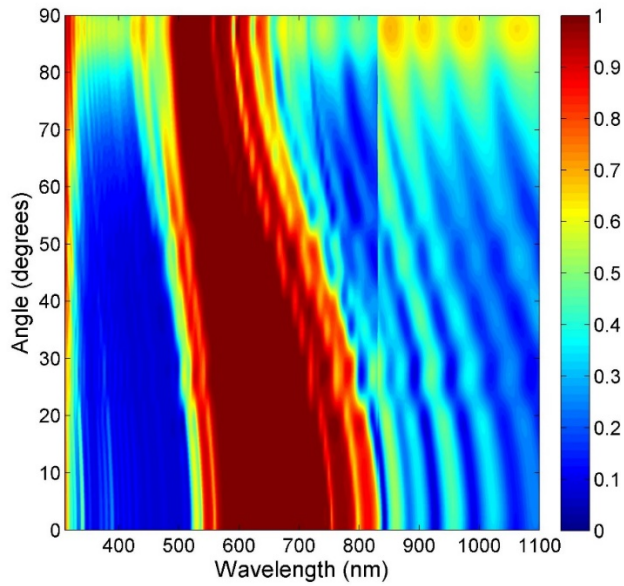

Figure 3.14: Measured reflectance of fabricated dielectric mirror

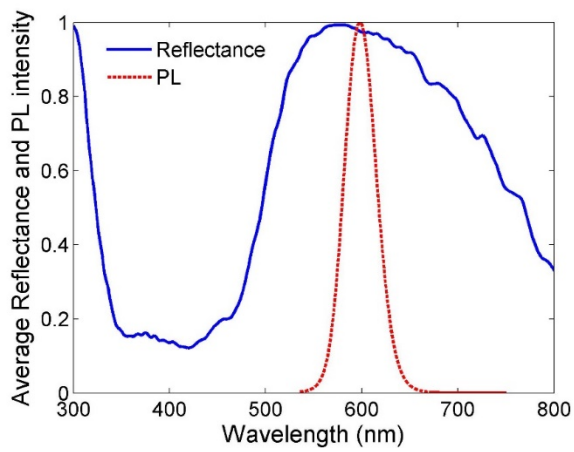

Figure 3.15: Angle-averaged reflectance of fabricated dielectric mirror
The photoluminescence (PL) spectrum is that of the particles used to make LSC devices in this study, normalized.

LSC devices were fabricated out of these mirrors and quantum dots according to the scheme from Figure 3.15. The device measurement scheme was exactly the same as the previous devices. The results of that measurement are shown in Figure 3.16. The overall EQE and collection efficiency of the device are low due to the small area covered by the single microcell. In the future, arrays of microcells could be integrated so as to capture more of the waveguided light with minimal shadowing. The champion device performance under AM1.5G illumination is summarized in Table 2, with current density (J)-voltage (V) curves shown in Figure 3.16. Both the J_{sc} and the V_{oc} of the microcell increase significantly upon integration with the LSC including the trench reflector, and increase further with the addition of the photonic mirror. The total J_{sc} of the Si microcell is 7.7

times higher after integration with the complete device. The spectral dependence of C is plotted in Fig. 3(c), and shows that the current enhancement originates from concentration of blue photons, the spectral region where the nanocrystals absorb. From 550 to 800 nm C is greatly suppressed, as this spectral region is reflected by the photonic mirror and prevented from entering the LSC. This loss is outweighed by the improvement in the concentration of blue photons as demonstrated by the total current enhancement.

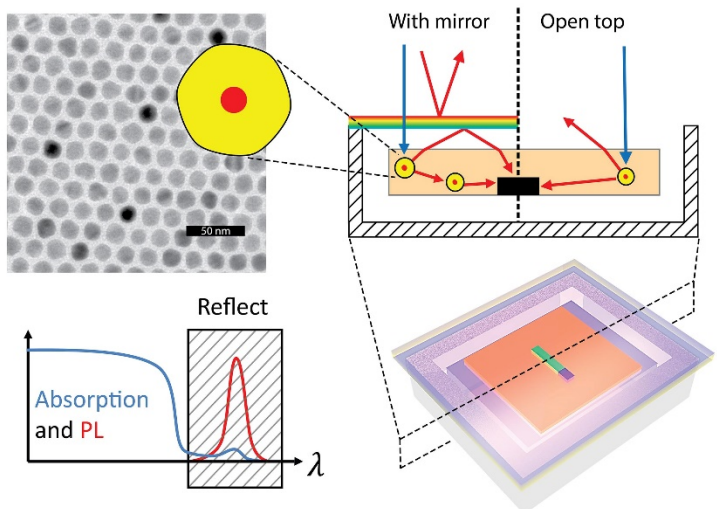

Figure 3.16: Device scheme for LSC with dielectric mirror
This scheme shows a representative quantum dot TEM image, the optical design, and the device design. The bottom and sides of the trench are coated in white scattering material (Spectralon from LabSphere). The small solar cell is incorporated into the waveguide, just as before, and the waveguide is once again a 180 um thick quartz sheet with a 30 um thick polymer quantum dot composite.

Testing Condition	J_{SC} (mA/cm^2) AM1.5G	Concentration λ = 350-500 nm	V_{OC} (V)	Fill Factor	Power (mW/cm^2)
μ-Si device	28.51	1	0.504	0.72	10.35
μ-Si device LSC + trench	149.3	18.9	0.569	0.64	54.37
μ-Si device LSC + trench + DBR	218.7	30.3	0.580	0.61	77.38

Table 2: Champion LSC device performance

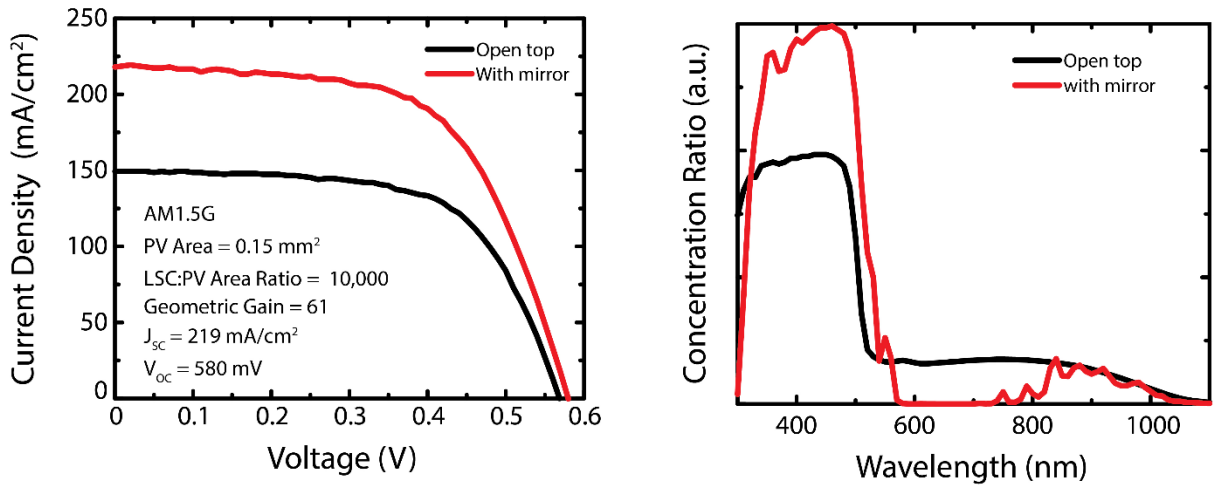

Figure 3.17: LSC device performance with dielectric mirror
J-V characteristics of the LSC device with and without the photonic mirror are plotted on the left. Concentration ratio as a function of excitation wavelength of the LSC-PV device with and without the photonic mirror are plotted on the right.

The optical density (OD) at 450 nm of the nanocrystal-polymer films was then varied from 0.1 to 1.2, and the LSCs were characterized under blue-filtered illumination. The highest concentration factor occurs when OD=0.65 (**Fig. 4(a)**). At lower OD, absorption of incident sunlight in the blue portion of the spectrum is diminished, while at higher OD reabsorption and scattering of luminesced photons decrease the optical efficiency. All samples demonstrate more than 60% enhancement in *C* after applying the photonic mirror except the control device (no QDs added in the polymer). The optimum *C* under the blue-filter illumination with the photonic mirror reaches 30.3, a value unprecedented in the LSC literature.

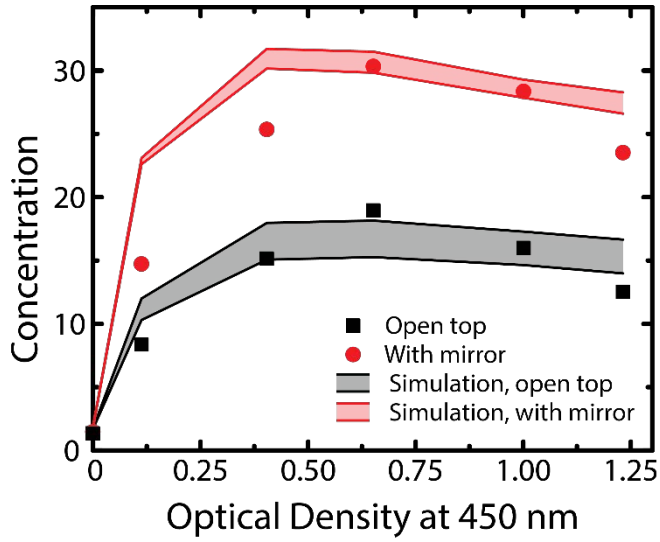

Figure 3.18: Champion LSC device performance with dielectric mirror
Varying the optical density results in a maximum concentration of 30.3 at OD of 0.65 at 450 nm. Without the mirror, the LSC still achieves concentration factor 18.

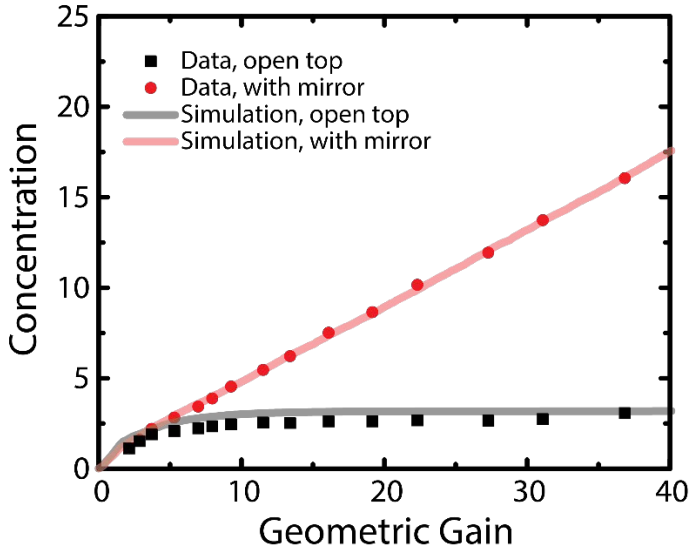

Figure 3.19: Photon transport measurement in cloudy LSC with mirror
Fabrication issues led to a cloudy polymer, which inhibit photon transport. With the mirror on top, the device is still able to collect photons over long distances.

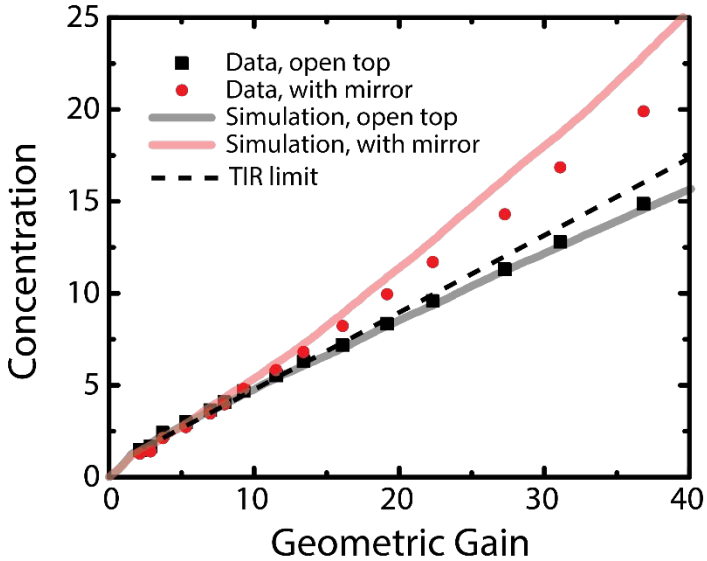

Figure 3.20: Photon transport measurements in clear LSC with mirror
The champion (OD=0.65) device is measured as a function of geometric gain. The TIR limit plotted here assumes a PLQY of 0.6 and a TIR efficiency of 0.72, and that the short distance behavior (G<5) is complicated by measurement issues.

To study the propagation of photons inside the LSC, we compared a sample with high internal scattering (Fig. 4(b), due to the absence of thorough QD cleaning before polymerization) to one with low scattering (Fig. 4(c)) (See Supporting Method S4 for details). Both samples had an optimal OD of 0.65 at 450 nm, and were measured under blue-filtered illumination with variable illumination spot diameter resulting in variable geometric gain *G* (the ratio of illuminated area to illuminated edge area).

Our definition of geometric gain (i.e. waveguide top area/edge area) is slightly different from previous literature reports, where the geometric gain is considered as a device property, and calculated as the ratio of illuminated area to solar cell area. And in the classic case where solar cells cover the sides and the whole LSC waveguide is illuminated from the top, these two definitions are practically identical. However, if we imagine a luminescent waveguide with no photovoltaic material at all, immediate confusion arises. It should be apparent that such a device does exhibit luminescent concentration, but that the concentration is not harvested and as such does no useful work. If one wanted to measure that concentration, one could place a very small optical detector inside the waveguide so as not to perturb the photon field too much. This is what we have done in this study. Such an embedded detector must have a well-understood wavelength-dependent response, geometry, and illumination pattern in order to use it to measure the concentration of photons. These conditions are all met for our detector.

Without the photonic mirror acting as a photon-recycling element, the sample with high scattering (Figure 3.18) shows a limited growth of *C* that quickly plateaus with increasing *G*, as luminesced photons are scattered out of the waveguide and lost. In comparison, the sample with low scattering exhibits a quasi-linear increase of *C* with *G*, as contributed by the uninterrupted TIR modes inside the waveguide.[20]

Adding the photonic mirror on top allows both non-TIR and scattered photons to be recycled and then to propagate inside the concentrator cavity before finally reaching the solar cell. As a result, the losses associated with scattering are strongly reduced, and photons are concentrated over distances much longer than the scattering length of the waveguide. In the high scattering case (Figure 3.18) *C* becomes quasi-linear with increasing *G*, and reaches 16 at *G*=37, nearly five times higher than without the mirror. This value is still smaller than that in the low scattering case (*C*=20), indicating that scattering loss is not completely mitigated as the mirror reflectivity diminishes at oblique angles. Measurement of the luminescent concentration factor of the high scattering sample with the dielectric mirror at *G*=61 resulted in *C*=26, only slightly reduced from the champion value of 30.3 for the non-scattering device. In the device with low scattering (Figure 3.19), *C* increases super-linearly with the illumination diameter, increasing faster than the TIR limit. This super-linearity marks the onset of a transition from ballistic, single-pass photon transport to diffusion-based transport afforded by photon-recycling.

Separately, the effect of the photonic mirror was quantified by measuring the optical trapping efficiency (η_{trap})—the fraction of photons that propagate to the edges of the waveguide (with no embedded photovoltaic microcell). Without the photonic mirror, $\eta_{trap}$is limited by the fraction (η_{TIR}) of photons initially trapped by total internal reflection (TIR) in a polymer with refractive index n

$$\eta_{trap} \leq \eta_{TIR} \ = \ (1 - n^{-2})^{\frac{1}{2}}$$

For the PLMA/QD composite (n =1.44), and $\eta_{TIR} = 0.72$. For a 30 µm thick luminescent film placed between two thin glass coverslips, η_{trap} averages around 66% (Fig. 2(d)), slightly lower than η_{TIR} due to scattering and reabsorption losses. Replacing both glass coverslips with photonic

mirrors, luminesced photons cannot escape out of the front and back surface of the waveguide, increasing η_{trap} to 82% (Fig. 2(d)), exceeding the value Snell's law would allow without the dielectric mirrors.

In conclusion, our results suggest that efficient trapping of luminescence with a dielectric mirror can keep the luminescence inside the cavity regardless of the optical clarity and smoothness of the waveguide. If the optical quality of the waveguide could truly be made irrelevant by the dielectric mirror, the fabrication of the devices could be simplified. We experimentally achieved luminescent solar concentration ratios over 30 while maintaining a high waveguide efficiency of 82%. This is due to the combination of designer nanocrystal lumophores with a photonic cavity that traps luminescence. The narrow emission linewidth of the nanocrystal lumophores enables the use of a highly reflective, wavelength-selective photonic mirror as the top surface of the cavity. In addition to improving the photon concentration ratio, the luminescence-trapping effect of the mirror also dramatically mitigates the detrimental effect of scattering.

The device fabricated here is tuned to utilize the blue portion of the spectrum due to the engineered absorption spectrum of the CdSe/CdS QDs. The system efficiency remains limited, as only one silicon microcell is utilized to detect rather than fully convert the luminescence in the waveguide. Using transfer-printing based assembly, however, arrays of these microscale devices could be embedded in the waveguide to dramatically enhance the PV conversion efficiency.[31]

Chapter 4 : Luminescent Solar Concentrators as Top Junctions for Silicon

As silicon prices have fallen, it has become increasingly clear that future solar panels will need to have both low cost and high efficiency. One promising strategy for achieving a higher efficiency is to use different parts of the solar spectrum in photovoltaic materials with varying bandgaps to minimize losses associated with carrier thermalization and incomplete photon absorption. For these multi-junction (MJ) PV devices, there is a strong need for developing low-cost, high-bandgap solar cells for efficient utilization of the high energy part of the solar spectrum. A luminescent solar concentrator could provide exactly this function, serving as the top junction in a multi-junction architecture by converting blue photons into guided luminescence. Due to the concentration effect, only small amounts of high-performing but expensive III-V photovoltaic materials are needed to collect the light from an inexpensive luminescent waveguide. Such a device requires high concentration factors to reduce the cost of the III-V photovoltaic material. High concentration also allows the Stokes Shift of the lumophore to be recovered in the operating voltage of the photovoltaic cell.

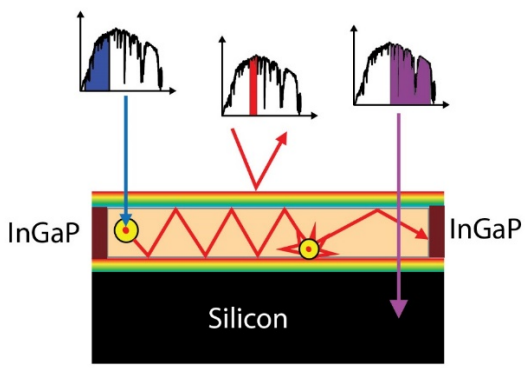

Figure 4.1: LSC on Silicon tandem device architecture
Photonic notch mirrors are used to enhance the performance of the LSC. When the mirrors are used, a small portion of the solar spectrum is reflected. When they are not used, that portion is transmitted to the silicon beneath the LSC.

4.1: Thermodynamics

It is possible to calculate the efficiency of this tandem device from thermodynamic first-principles following the Shockley-Quessier analysis with some minor modifications. First, it is important to calculate the 2-junction photovoltaic device efficiency limit without the current matching criterion. The result of this calculation is shown in Figure 4.2. The maximum efficiency exceeds 44%, and is achieved for a low bandgap of around 0.95 eV and a high bandgap of 1.75 eV.

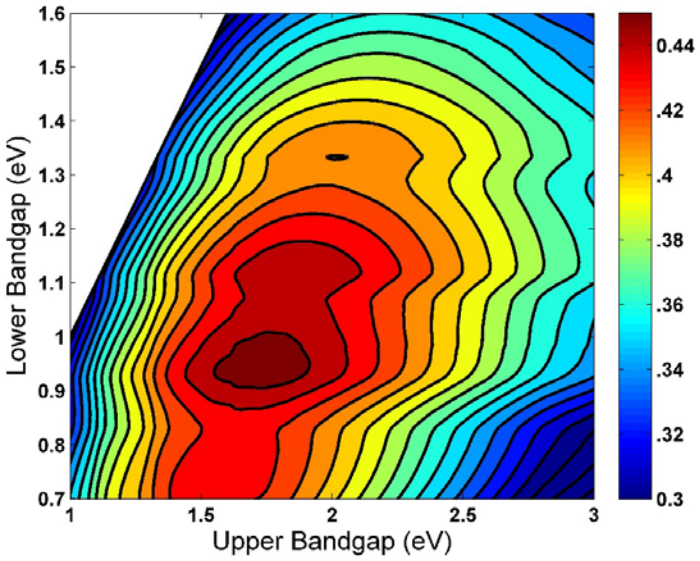

Figure 4.2: Two-junction PV thermodynamic limit

This calculation, while thermodynamically accurate for two semiconductors stacked vertically, is not accurate when the top junction requires a photonic mirror that will partially shadow the bottom junction. In that case, some current is lost from the bottom cell. A hypothetical perfect notch filter can be applied, and the efficiency can be calculated. Additionally, the external radiative efficiency is left as a parameter due to the inherent difficulty of producing high voltage in a LSC device. The results of this computation are shown in Figure 4.3. In these computations, the ERE of the silicon was assumed to be 1%, which is consistent with experimentally achieved values.

The results show that a narrow reflection bandwidth is required in order to avoid too much shadowing. Quantum dots would require a reflection band of at least 50 nm width due to the homogenous line width which is around 18-19 nm full-width-half-max. Organic dyes are typically much broader, so they would not do well in this application. Significantly narrower emission peaks have been measured for lanthanide ions, but to date there is no efficient way to transfer energy from broadband strong absorbers to lanthanide emitters. The development of such a lumophore with high luminescence efficiency would be of great benefit to these LSC tandem devices.

Further, in Figure 4.3, two conditions are considered. In one, InGaP is used as the top junction photovoltaic material. In the other, GaAs is used. The CdSe/CdS lumophores described in this dissertation are well matched to InGaP, which has a bandgap of around 1.9 eV (and can be tuned based on the In to Ga ratio). There is no comparably high luminescence efficiency lumophore in existence today that is matched to GaAs. The development of such a lumophore would enable these devices to use GaAs instead of InGaP. While the thermodynamic limits of the two cases are similar, GaAs is much more widely available and inexpensive due to the efforts of the company Alta Devices, which is commercializing its world record GaAs photovoltaic cells.

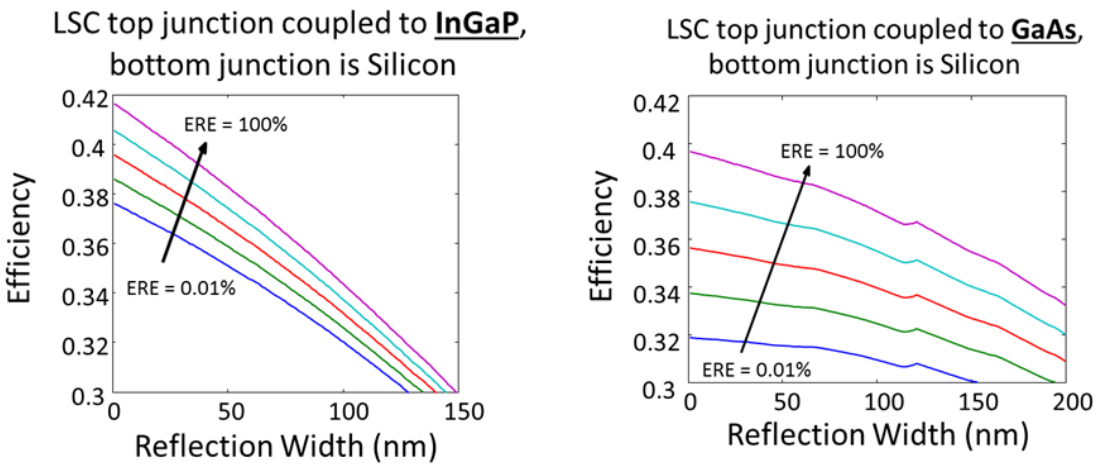

Figure 4.3: Thermodynamic efficiency of the LSC-Silicon tandem
The bandgap of the photovoltaic in the LSC is held constant, and a variable width notch filter is applied, extending toward higher energy from the bandgap of the III-V cell in the LSC. Varying the ERE of the III-V changes the voltage, and varying the reflection width changes the current. The power output of the silicon is constant for each graph.

4.2: Performance predictions for real devices

The thermodynamic limits described above are the most optimistic estimate of the PV power production by these devices. They do not account for the non-idealities that will likely be present in a fabricated device. In order to estimate the power production from real devices, a full device model was built utilizing the photon-flow model shown in Figure 4.4. A description of the items in the model, and estimates for their values, can be found in Table 3 and Table 4. The finite element optical model from Chapter 3 was used to estimate the LSC efficiency. Voltage behavior for the Silicon, GaAs, and InGaP cell were taken from record literature devices.[66,67]

Using this technique, efficiency of 24-30% is predicted for the LSC+InGaP on Si, and 27-34% is predicted for the LSC+GaAs on Si. The design rules shown here are that extremely high mirror reflectivity is needed to achieve high LSC efficiency (R>99%), high transmission in the pass band is required (T>95%), high luminescence quantum yield is needed (QY>98%), and photovoltaic cells must also be excellent. If all of these criteria can be met, efficiency exceeding 30% may be possible. The production of prototypes and test structures toward building these devices and achieving these high efficiencies is the subject of future research.

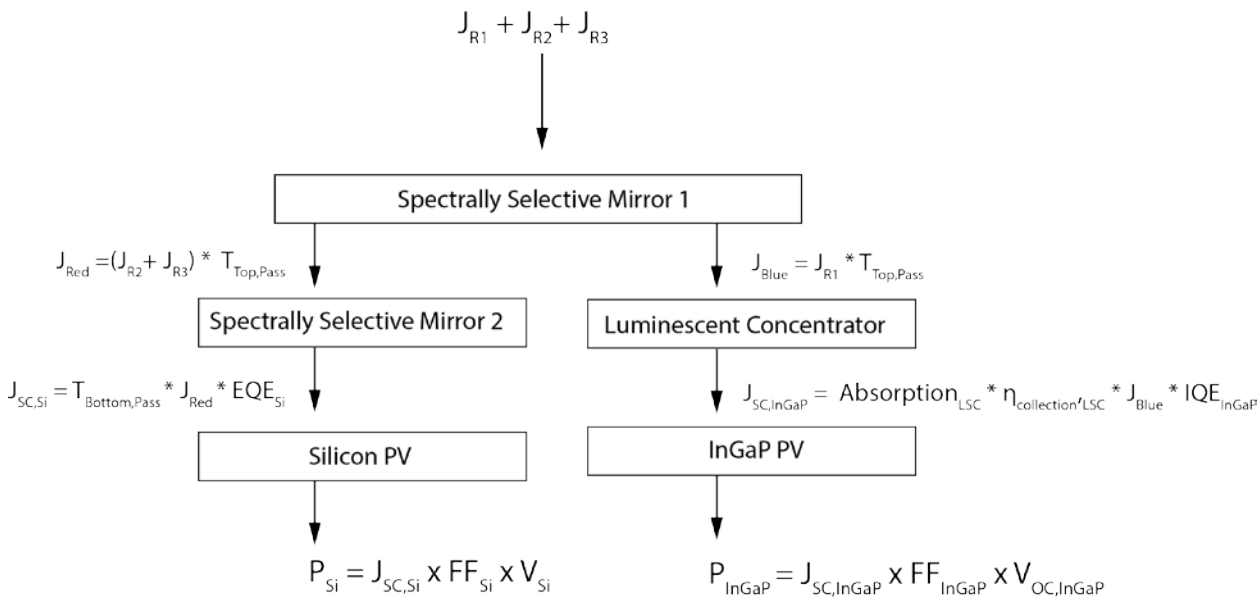

Figure 4.4: Photon flow model for LSC-Si tandem device
Arrows indicate flows of photons. High energy photons are converted by the Luminescent Concentrator into luminescence and then converted into power by the InGaP PV. Lower energy incident photons are converted into power by the Silicon PV after transmitting through both Spectrally Selective Mirrors.

Parameter	Symbol	Optimistic Value	Conservative Value
Solar photon flux above the CdS bandgap	J_{R1}	77.4 A / m²	
Solar photon flux between CdS bandgap and mirror reflectance band	J_{R2}	68.9 A / m²	
Solar photon flux between mirror reflectance band and silicon bandgap	J_{R3}	244.8 A / m²	
Ratio of electrical current produced to absorbed photons for InGaP cell	IQE_{InGaP}	1	0.99
Ratio of electrical current produced to incident photons for silicon cell	EQE_{Si}	1	0.95
Transmittance of top mirror in pass band	$T_{Top,Pass}$	1	0.97
Transmittance of bottom mirror in pass band	$T_{Bottom,Pass}$	1	0.97
Open circuit voltage of silicon cell under AM1.5G	$V_{OC-Si,AM1.5G}$	0.735 V	0.7 V
Open circuit voltage of InGaP cell under AM1.5G	$V_{OC-InGaP,AM1.5G}$	1.48 V	1.4 V
Open circuit voltage of silicon cell under the LSC	V_{OC-Si}	0.727 V	0.7 V
Open circuit voltage of InGaP cell in the LSC	$V_{OC-InGaP}$	1.597 V	1.517 V
short circuit current of the silicon cell	J_{SC-Si}	313.7 A / m²	280.4 A / m²
photon collection efficiency of the LSC	$\eta_{collection,LSC}$	0.98	0.95
Fraction of solar photons absorbed above the CdS bandgap in the LSC waveguide	$Absorption_{LSC}$	0.99	0.95
Short circuit current of the InGaP cell	$J_{SC-InGaP}$	75.3 A / m²	65.7 A /m²
Fill factor of the silicon cell	FF_{Si}	0.837	0.8
Fill factor of the InGaP cell	FF_{InGaP}	0.88	0.85
Incident solar power	P_{solar}	1000 W / m²	
Power output of the silicon cell	P_{Si}	**190.8 W / m²**	**155.1 W / m²**
Power output of the InGaP solar cells	P_{InGaP}	**105.8 W / m²**	**84.7 W / m²**
Efficiency of power generation	$\eta_{Harvest,DC}$	**29.7%**	**24.0%**

Table 3: Power generation estimates for LSC+InGaP-Si tandem

Parameter	***Symbol***	***Optimistic Value***	***Conservative Value***
Solar photon flux above the IR QD bandgap	J_{R1}	239.9 A / m²	
Solar photon flux between IR QD bandgap and mirror reflectance band	J_{R2}	33.2 A / m²	
Solar photon flux between mirror reflectance band and silicon bandgap	J_{R3}	110.0 A / m²	
Ratio of electrical current produced to absorbed photons for GaAs cell	IQE_{InGaP}	1	0.99
Ratio of electrical current produced to incident photons for silicon cell	EQE_{Si}	1	0.95
Transmittance of top mirror in pass band	$T_{bottom,pass}$	1	0.97
Transmittance of bottom mirror in pass band	$R_{bottom,pass}$	1	0.97
Open circuit voltage of silicon cell under AM1.5G	$V_{OC-Si,AM1.5G}$	0.735 V	0.7 V
Open circuit voltage of GaAs cell under AM1.5G	$V_{OC-GaAs,AM1.5G}$	1.11 V	1.05 V
Open circuit voltage of silicon cell under the LSC	V_{OC-Si}	0.706 V	0.671 V
Open circuit voltage of GaAs cell in the LSC	$V_{OC-GaAs}$	1.227 V	1.167 V
short circuit current of the silicon cell	J_{SC-Si}	143.2 A / m²	128.0 A / m²
photon collection efficiency of the LSC	$\eta_{collection,LSC}$	0.98	0.95
Fraction of solar photons absorbed above the CdS bandgap in the LSC waveguide	$Absorption_{LSC}$	0.99	0.95
Short circuit current of the GaAs cell	$J_{SC-GaAs}$	233.1 A / m²	203.5 A /m²
Fill factor of the silicon cell	FF_{Si}	0.837	0.8
Fill factor of the GaAs cell	FF_{GaAs}	0.88	0.85
Incident solar power	P_{solar}	1000 W / m²	
Power output of the silicon cell	$\boldsymbol{P_{Si}}$	**84.6 W / m²**	**68.7 W / m²**
Power output of the GaAs solar cells	$\boldsymbol{P_{GaAs}}$	**251.8 W / m²**	**201.9 W / m²**
Efficiency of power generation	$\boldsymbol{\eta_{Harvest,DC}}$	**33.6%**	**27.1%**

Table 4: Power generation estimates for LSC+GaAs-Si tandem

References

(1) Chapin, D. M.; Fuller, C. S.; Pearson, G. L. A New Silicon P-N Junction Photocell for Converting Solar Radiation into Electrical Power. *J. Appl. Phys.* **1954**, *25* (5), 676–677.

(2) Shockley, W.; Queisser, H. J. Detailed Balance Limit of Efficiency of P-N Junction Solar Cells. *J. Appl. Phys.* **1961**, *32* (3), 510.

(3) Conibeer, G. Third Generation Photovoltaics. *Rev. Lit. Arts Am.* **2007**, *10* (11), 42–50.

(4) Green, M. A. Photovoltaics: Technology Overview. *Energy Policy* **2000**, *28* (14), 989–998.

(5) Goetzberger, A.; Greubel, W. Solar Energy Conversion with Fluorescent Collectors. *Appl. Phys.* **1977**, *14*, 123–139.

(6) Batchelder, J. S.; Zewail, A. H.; Cole, T. Luminescent Solar Concentrators. 1: Theory of Operation and Techniques for Performance Evaluation. *Appl. Opt.* **1979**, *18* (18), 3090–3110.

(7) Batchelder, J. S.; Zewail, A. H.; Cole, T. Luminescent Solar Concentrators. 2: Experimental and Theoretical Analysis of Their Possible Efficiencies. *Appl. Opt.* **1981**, *20* (21), 3733–3754.

(8) Yablonovitch, E. Thermodynamics of the Fluorescent Planar Concentrator. *J. Opt. Soc. Am.* **1980**, *70* (11), 1362.

(9) Debije, M. G.; Verbunt, P. P. C. Thirty Years of Luminescent Solar Concentrator Research: Solar Energy for the Built Environment. *Adv. Energy Mater.* **2012**, *2* (1), 12–35.

(10) Goldschmidt, J. C.; Peters, M.; Gutmann, J.; Steidl, L.; Zentel, R.; Bläsi, B.; Hermle, M.; Chemie, O.; Mainz, U. Increasing Fluorescent Concentrator Light Collection Efficiency by Restricting the Angular Emission Characteristic of the Incorporated Luminescent Material - the “Nano-Fluko” Concept. *Proc. SPIE* **2010**, *7725*, 77250.

(11) Bradshaw, L. R.; Knowles, K. E.; McDowall, S.; Gamelin, D. R. Nanocrystals for

Luminescent Solar Concentrators. *Nano Lett.* **2015**, *15* (2), 1315–1323.

(12) Chatten, A. J.; Barnham, K. W. J.; Buxton, B. F.; Ekins-Daukes, N. J.; Malik, M. a. Quantum Dot Solar Concentrators. *Semiconductors* **2004**, *38* (8), 909–917.

(13) Debije, M. G.; Teunissen, J.-P.; Kastelijn, M. J.; Verbunt, P. P. C.; Bastiaansen, C. W. M. The Effect of a Scattering Layer on the Edge Output of a Luminescent Solar Concentrator. *Sol. Energy Mater. Sol. Cells* **2009**, *93* (8), 1345–1350.

(14) Debije, M. G.; Van, M.-P.; Verbunt, P. P. C.; Kastelijn, M. J.; van der Blom, R. H. L.; Broer, D. J.; Bastiaansen, C. W. M. Effect on the Output of a Luminescent Solar Concentrator on Application of Organic Wavelength-Selective Mirrors. *Appl. Opt.* **2010**, *49* (4), 745–751.

(15) Krumer, Z.; Pera, S. J.; van Dijk-Moes, R. J. A.; Zhao, Y.; de Brouwer, A. F. P.; Groeneveld, E.; Van Sark, W. G. J. H. M.; Schropp, R. E. I.; de Mello Donegá, C. Tackling Self-Absorption in Luminescent Solar Concentrators with Type-II Colloidal Quantum Dots. *Sol. Energy Mater. Sol. Cells* **2013**, *111*, 57–65.

(16) Roncali, J.; Garnier, F. Photon-Transport Properties of Luminescent Solar Concentrators: Analysis and Optimization. *Appl. Opt.* **1984**, *23* (16), 2809.

(17) Bomm, J.; Büchtemann, A.; Chatten, A. J.; Bose, R.; Farrell, D. J.; Chan, N. L. A.; Xiao, Y.; Slooff, L. H.; Meyer, T.; Meyer, A.; et al. Fabrication and Full Characterization of State-of-the-Art Quantum Dot Luminescent Solar Concentrators. *Sol. Energy Mater. Sol. Cells* **2011**, *95* (8), 2087–2094.

(18) van Sark, W. G. J. H. M.; Barnham, K. W. J.; Slooff, L. H.; Chatten, A. J.; Büchtemann, A.; Meyer, A.; McCormack, S. J.; Koole, R.; Farrell, D. J.; Bose, R.; et al. Luminescent Solar Concentrators--a Review of Recent Results. *Opt. Express* **2008**, *16* (26), 21773–21792.

(19) Giebink, N. C.; Wiederrecht, G. P.; Wasielewski, M. R. Resonance-Shifting to Circumvent Reabsorption Loss in Luminescent Solar Concentrators. *Nat. Photonics* **2011**, *5* (11), 694–701.

(20) Bronstein, N. D.; Li, L.; Xu, L.; Yao, Y.; Ferry, V. E.; Alivisatos, A. P.; Nuzzo, R. G.

Luminescent Solar Concentration with Semiconductor Nanorods and Transfer-Printed Micro-Silicon Solar Cells. *ACS Nano* **2014**, *8* (1), 44–53.

(21) Bronstein, N. D.; Yao, Y.; Xu, L.; O'Brien, E.; Powers, A. S.; Ferry, V. E.; Alivisatos, A. P.; Nuzzo, R. G. Quantum Dot Luminescent Concentrator Cavity Exhibiting 30-Fold Concentration. *ACS Photonics* **2015**, *ASAP*.

(22) Roncali, J.; Garnier, F. New Luminescent Back Reflectors for the Improvement of the Spectral Response and Efficiency of Luminescent Solar Concentrators. *Sol. Cells* **1984**, *13* (2), 133–143.

(23) Meinardi, F.; Colombo, A.; Velizhanin, K. A.; Simonutti, R.; Lorenzon, M.; Beverina, L.; Viswanatha, R.; Klimov, V. I.; Brovelli, S. Large-Area Luminescent Solar Concentrators Based on "Stokes-Shift-Engineered" Nanocrystals in a Mass-Polymerized PMMA Matrix. *Nat. Photonics* **2014**, *8* (May), 392–399.

(24) Coropceanu, I.; Bawendi, M. G. Core/shell Quantum Dot Based Luminescent Solar Concentrators with Reduced Reabsorption and Enhanced Efficiency. *Nano Lett.* **2014**, *14* (7), 4097–4101.

(25) Wurfel, P. *Physics of Solar Cells*, 2nd ed.; WILEY-VCH Verlag Gmbh & Co. KGaA: Weinheim, 2009.

(26) van Roosbroeck, W.; Shockley, W. Photon-Radiative Recombination of Electrons and Holes in Germanium. *Phys. Rev.* **1954**, *94* (6), 1558–1560.

(27) Miller, O.; Yablonovitch, E. Detailed Balance Solar Cell Efficiency Limits for Internal Fluorescence Yield Slightly Less Than 100 %. *Cell* **2010**, No. 1, 5–7.

(28) Miller, O. D.; Yablonovitch, E.; Kurtz, S. R. Strong Internal and External Luminescence as Solar Cells Approach the Shockley-Queisser Limit. *IEEE J. Photovoltaics* **2012**, *2* (3), 303–311.

(29) Slooff, L. H.; Bende, E. E.; Burgers, A. R.; Budel, T.; Pravettoni, M.; Kenny, R. P.; Dunlop, E. D.; Büchtemann, A. A Luminescent Solar Concentrator with 7.1% Power Conversion Efficiency. *Phys. status solidi* **2008**, *2* (6), 257–259.

(30) Currie, M. J.; Mapel, J. K.; Heidel, T. D.; Goffri, S.; Baldo, M. A. High-Efficiency Organic Solar Concentrators for Photovoltaics. *Science* **2008**, *321* (5886), 226–228.

(31) Yoon, J.; Li, L.; Semichaevsky, A. V; Ryu, J. H.; Johnson, H. T.; Nuzzo, R. G.; Rogers, J. a. Flexible Concentrator Photovoltaics Based on Microscale Silicon Solar Cells Embedded in Luminescent Waveguides. *Nat. Commun.* **2011**, *2*, 343.

(32) Semichaevsky, A. V; Johnson, H. T.; Yoon, J.; Nuzzo, R. G.; Li, L.; Rogers, J. Theory for Optimal Design of Waveguiding Light Concentrators in Photovoltaic Microcell Arrays. *Appl. Opt.* **2011**, *50* (17), 2799–2808.

(33) Sheng, X.; Shen, L.; Kim, T.; Li, L.; Wang, X.; Dowdy, R.; Froeter, P.; Shigeta, K.; Li, X.; Nuzzo, R. G.; et al. Doubling the Power Output of Bifacial Thin-Film GaAs Solar Cells by Embedding Them in Luminescent Waveguides. *Adv. Energy Mater.* **2013**, *3* (8), 991–996.

(34) Earp, A. A.; Smith, G. B.; Franklin, J.; Swift, P. Optimisation of a Three-Colour Luminescent Solar Concentrator Daylighting System. *Sol. Energy Mater. Sol. Cells* **2004**, *84* (1-4), 411–426.

(35) Chatten, A. J.; Barnham, K. W. J.; Buxton, B. F.; Ekins-Daukes, N. J.; Malik, M. A. A New Approach to Modelling Quantum Dot Concentrators. *Sol. Energy Mater. Sol. Cells* **2003**, *75* (3-4), 363–371.

(36) Slooff, L. H.; Burgers, a. R.; Debije, M. G. Reduction of Escape Cone Losses in Luminescent Solar Concentrators with Cholesteric Mirrors. *Proc. SPIE* **2008**, *7043*, 704306–704306 – 7.

(37) Chaudhuri, R. G.; Paria, S.; Ghosh Chaudhuri, R.; Paria, S. Core/shell Nanoparticles: Classes, Properties, Synthesis Mechanisms, Characterization, and Applications. *Chem. Rev.* **2012**, *112* (4), 2373–2433.

(38) Talapin, D. V; Nelson, J. H.; Shevchenko, E. V; Aloni, S.; Sadtler, B.; Alivisatos, a P. Seeded Growth of Highly Luminescent CdSe/CdS Nanoheterostructures with Rod and Tetrapod Morphologies. *Nano Lett.* **2007**, *7* (10), 2951–2959.

(39) Carbone, L.; Nobile, C.; De Giorgi, M.; Sala, F. Della; Morello, G.; Pompa, P.; Hytch, M.; Snoeck, E.; Fiore, A.; Franchini, I. R.; et al. Synthesis and Micrometer-Scale Assembly of Colloidal CdSe/CdS Nanorods Prepared by a Seeded Growth Approach. *Nano Lett.* **2007**, *7* (10), 2942–2950.

(40) Chen, O.; Zhao, J.; Chauhan, V. P.; Cui, J.; Wong, C.; Harris, D. K.; Wei, H.; Han, H.; Fukumura, D.; Jain, R. K.; et al. Compact High-Quality CdSe-CdS Core-Shell Nanocrystals with Narrow Emission Linewidths and Suppressed Blinking. *Nat. Mater.* **2013**, *12* (5), 445–451.

(41) Chan, E. M.; Xu, C.; Mao, A. W.; Han, G.; Owen, J. S.; Cohen, B. E.; Milliron, D. J. Reproducible, High-Throughput Synthesis of Colloidal Nanocrystals for Optimization in Multidimensional Parameter Space. *Nano Lett.* **2010**, *10* (5), 1874–1885.

(42) Talapin, D. V.; Koeppe, R.; Götzinger, S.; Kornowski, A.; Lupton, J. M.; Rogach, A. L.; Benson, O.; Feldmann, J.; Weller, H. Highly Emissive Colloidal CdSe/CdS Heterostructures of Mixed Dimensionality. *Nano Lett.* **2003**, *3* (12), 1677–1681.

(43) Liu, H.; Owen, J. S.; Alivisatos, a P. Mechanistic Study of Precursor Evolution in Colloidal Group II-VI Semiconductor Nanocrystal Synthesis. *J. Am. Chem. Soc.* **2007**, *129* (2), 305–312.

(44) Jain, P. K.; Beberwyck, B. J.; Fong, L.-K.; Polking, M. J.; Alivisatos, A. P. Highly Luminescent Nanocrystals From Removal of Impurity Atoms Residual From Ion-Exchange Synthesis. *Angew. Chemie Int. Ed.* **2012**, *51* (10), 2387–2390.

(45) Yu, W. W.; Qu, L.; Guo, W.; Peng, X. Experimental Determination of the Extinction Coefficient of CdTe, CdSe, and CdS Nanocrystals. *Chem. Mater.* **2003**, *15* (14), 2854–2860.

(46) Ninomiya, S.; Adachi, S. Optical Properties of Wurtzite. *Electronics* **1995**, *78* (2), 1183–1190.

(47) Yablonovitch, E. Statistical Ray Optics. *America (NY).* **1982**, *72* (7), 899–907.

(48) Bohren, C. F.; Huffman, D. R. *Absorption and Scattering of Light by Small Particles*; WILEY-VCH Verlag GmbH & Co. KGaA: Weinheim, 1983.

(49) Palik, E. D. *Handbook of Optical Constants of Solids*; Academic Press: Burlington, 1997.

(50) Moreels, I.; Allan, G.; De Geyter, B.; Wirtz, L.; Delerue, C.; Hens, Z. Dielectric Function of Colloidal Lead Chalcogenide Quantum Dots Obtained by a Kramers-Krönig Analysis of the Absorbance Spectrum. *Phys. Rev. B* **2010**, *81* (23), 235319.

(51) Jasieniak, J.; Smith, L.; Embden, J. Van; Mulvaney, P. Re-Examination of the Size-Dependent Absorption Properties of CdSe Quantum Dots. **2009**, 19468–19474.

(52) Miller, O. D.; Yablonovitch, E.; Kurtz, S. R. Intense Internal and External Fluorescence as Solar Cells Approach the Shockley-Queisser Efficiency Limit. **2011**, 2012.

(53) Rau, U.; Einsele, F.; Glaeser, G. C. Efficiency Limits of Photovoltaic Fluorescent Collectors. *Appl. Phys. Lett.* **2005**, *87* (17), 1–3.

(54) Ries, H.; Smestad, G. P.; Winston, R. Thermodynamics of Light Concentrators. In *Proceedings of SPIE*; 1991; Vol. 1528, p 7.

(55) Bose, R.; Farrell, D. J.; Chatten, A. J.; Pravettoni, M.; Buchtemann, A.; Quilitz, J.; Fiore, A.; Manna, L.; Barnham, K. W. J. Luminescent Solar Concentrators: Nanorods and Raytrace Modeling. *Conf. Rec. IEEE Photovolt. Spec. Conf.* **2008**, 2–6.

(56) Bronstein, N. D.; Li, L.; Xu, L.; Yao, Y.; Ferry, V. E.; Alivisatos, a. P.; Nuzzo, R. G.; Brueckner, E.; Alivisatos, a. P.; Nuzzo, R. G.; et al. Luminescent Solar Concentration with Semiconductor Nanorods and Transfer-Printed Micro-Silicon Solar Cells. *ACS Nano* **2014**, *8* (1), 44–53.

(57) Flores Daorta, S.; Proto, A.; Fusco, R.; Claudio Andreani, L.; Liscidini, M. Cascade Luminescent Solar Concentrators. *Appl. Phys. Lett.* **2014**, *104* (15), 153901.

(58) Yablonovitch, E. Inhibited Spontaneous Emission in Solid-State Physics and Electronics. *Phys. Rev. Lett.* **1987**, *58* (20), 2059–2062.

(59) Yablonovitch, E. Photonic Band-Gap Structures. *J. Opt. Soc. Am. B* **1993**, *10* (2), 283.

(60) Johnson, S. G.; Joannopoulos, J. D. Introduction to Photonic Crystals: Bloch's Theorem, Band Diagrams, and Gaps (but No Defects). *Photonic Cryst. Tutor.* **2003**, No. February, 1–16.

(61) Joannopoulos, J. J. D.; Johnson, S.; Winn, J. N. J.; Meade, R. R. D. *Photonic Crystals: Molding the Flow of Light*; 2008.

(62) Winn, J. N.; Fink, Y.; Fan, S.; Joannopoulos, J. D. Omnidirectional Reflection from a One-Dimensional Photonic Crystal. *Opt. Lett.* **1998**, *23* (20), 1573–1575.

(63) Fink, Y.; Winn, J. N.; Fan, S.; Chen, C.; Michel, J.; Joannopoulos, J. D.; Thomas, E. L. A Dielectric Omnidirectional Reflector. *Science (80-.).* **1998**, *282* (5394), 1679–1682.

(64) Marshall, L. F.; Cui, J.; Brokmann, X.; Bawendi, M. G. Extracting Spectral Dynamics from Single Chromophores in Solution. *Phys. Rev. Lett.* **2010**, *105* (5), 053005.

(65) Cui, J.; Beyler, A. P.; Marshall, L. F.; Chen, O.; Harris, D. K.; Wanger, D. D.; Brokmann, X.; Bawendi, M. G. Direct Probe of Spectral Inhomogeneity Reveals Synthetic Tunability of Single-Nanocrystal Spectral Linewidths. *Nat. Chem.* **2013**, *5* (7), 602–606.

(66) Geisz, J. F.; Steiner, M. A.; García, I.; Kurtz, S. R.; Friedman, D. J. Enhanced External Radiative Efficiency for 20.8% Efficient Single-Junction GaInP Solar Cells. *Appl. Phys. Lett.* **2013**, *103* (4), 2011–2016.

(67) Green, M. A.; Emery, K.; Hoshikawa, Y.; Warta, W.; Dunlop, E. D. Solar Cell Efficiency Tables (Version 45). *Prog. Photovoltaics Res. Appl.* **2015**, *23*, 1.